JOURNAL OF SPACECRAFT AND ROCKETS
Vol. 46, No. 1, January–February 2009

Modal Linear Stability of the Near-Wall Flow on a Hypersonic Forebody

M. Ferrier,* I. Fedioun,† E. Orlik,‡ and D. Davidenko§
Centre National de la Recherche Scientifique, 45071 Orléans Cedex 2, France

DOI: 10.2514/1.37093

The three-dimensional modal linear stability analysis is performed for the near-wall flow of a full-scale generic hypersonic vehicle forebody at flight Mach numbers 4, 6, and 8, at different angles of attack. The mean flow is computed with a Navier–Stokes commercial code. A physically sound, computationally efficient original method is proposed to define the integration path in the e^N method. It has a significant impact on the computed N factors. The entropy-layer effect on the flow instability is analyzed in the framework of Lees and Lin's asymptotic theory. The entropy layer introduces an additional unstable mode, for which $N \approx 4$. Results show that crossflow instability is dominant at Mach 6 and 8, whereas Mack's oblique first mode prevails at Mach 4. This mode is stabilized by a radiating wall, compared with an adiabatic one. Mack's second mode is also present at Mach 8. In any case, none of the instability modes that have been found is strong enough to provoke a natural transition in flight by itself: computed N factors do not exceed 10. Attempts to correlate the results with the $Re_\theta/M^e = \text{Const}$ criterion are discussed.

Nomenclature

a	=	speed of sound, m/s
C_p,	=	heat capacity at constant pressure, J/kg · K
C_v	=	heat capacity at constant volume, J/kg · K
f	=	frequency, Hz
h	=	enthalpy per unit mass, J/kg
k	=	thermal conductivity, W/m · K
$\boldsymbol{k}$	=	wave vector (real), 1/m
P	=	pressure, Pa
r	=	$C_p - C_v$, gas constant, J/kg · K
T	=	temperature, K
t	=	time, s
U, V, W	=	mean-flow components along x, y, and z, m/s
$\boldsymbol{V_g}$	=	group velocity vector, m/s
V_φ	=	phase velocity, m/s
W_α	=	molecular weight of species α, kg/kmol
X, Y, Z	=	coordinates in the global reference frame attached to the vehicle, m
x, y, z	=	streamwise, transverse (normal to the wall), and spanwise coordinates, m
X_α	=	mole fraction of species α
α, β	=	wave numbers (complex) in the x and z directions, 1/m
δ^*	=	displacement thickness, m
θ	=	momentum thickness, m
θ_g	=	direction of $\boldsymbol{V_g}$
μ	=	viscosity, kg/m · s
ν	=	μ/ρ, diffusivity, m^2/s
ρ	=	density, kg/m^3
$\boldsymbol{\sigma}$	=	amplification vector (real), 1/m
χ	=	compressibility factor
ψ	=	direction of $\boldsymbol{k}$
$\bar{\psi}$	=	direction of $\boldsymbol{\sigma}$
ω	=	(real) pulsation, 1/s

Subscripts

M	=	maximum value (envelope method)
u	=	unity
w	=	value at the wall
∞	=	value at infinity, static value

Superscripts

e	=	value in the freestream, outside the boundary layer
N	=	exponent in the e^N method

I. Introduction

THE recent regain of interest for hypersonic airbreathing scramjet-powered vehicles has led us to consider the laminar-turbulent transition prediction from an engineering point of view, that is, on full-scale 3-D realistic configurations. Indeed, for the air inlet to be well adapted, it is highly desirable for the boundary layer (BL) developing under the forebody to be turbulent in order to avoid flow separation due to strong adverse pressure gradients. One way to fix the problem is to trigger the transition with distributed roughnesses of various shapes and heights on the forebody. This implies running experiments in a conventional or quiet hypersonic wind tunnel to see what is the most efficient [1,2], although this is very costly. Another way is to try to predict the onset (or not) of the natural transition from empirical criterion, like the National Aerospace Plane (NASP) criterion, is $Re_\theta/M^e = \text{Const}$ (150 ∼ 500, with or without bluntness correction [3]), but this is only a first step, giving a global trend, and highly questionable [4,5].

More accurate methods are based on the knowledge of the mechanisms involved in the transition process. Understanding these mechanisms is still a challenging task in supersonic and hypersonic flows, after more than half a century of intensive research. Since the funding paper by Lees and Lin [6], and further developments by Mack [7,8], Malik [9], and others, numerous experimental and numerical parametric studies on transition in hypersonic flows have been done for flat plates or cones. The effects of Mach and Reynolds numbers, leading-edge bluntness, and angle of attack (AOA), have

Presented as Paper 2599 at the 15th AIAA International Space Planes and Hypersonic Systems and Technologies Conference, Dayton, OH, 28 April–1 May 2008; received 11 February 2008; revision received 4 July 2008; accepted for publication 7 July 2008.

*Ph.D. Student, Institut de Combustion, Aérothermique, Réactivité et Environnement, 1C Avenue de la Recherche Scientifique, Orléans, France. Student Member AIAA .

†Associate Professor, University of Orléans, France.

‡Ph.D. Student, Institut de Combustion, Aérothermique, Réactivité et Environnement, Orléans, France.

§Senior Research Associate, Institut de Combustion, Aérothermique, Réactivité et Environnement, Orléans, France. Member AIAA.

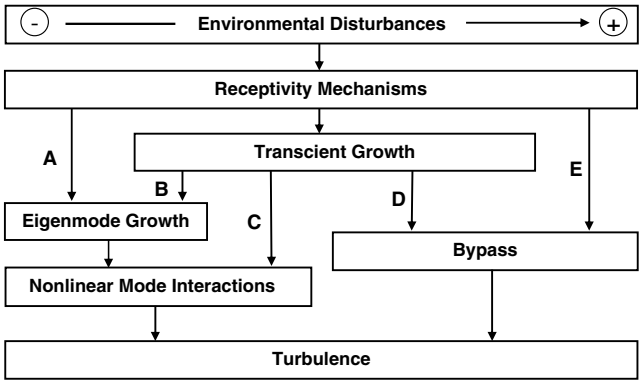

Fig. 1 Paths to turbulence in wall layers.

been investigated. A recent review has been done by Schneider [10] (see also [11]). Figure 1, taken from Reshotko [12], illustrates several paths to turbulence for wall-bounded flows, according to the level of external disturbances. In any case, disturbances have to first enter the wall layer through receptivity mechanisms, which can be investigated through direct numerical simulation [13]. In the case of low amplitude perturbations, path A is the familiar modal growth of Tollmien–Schlichting (TS)-like waves, the first of which have been studied by pioneering authors. At higher perturbation level, transient or nonmodal (algebraic) growth begins to play a role. It may either be followed by an exponential decay and then by a modal amplification (path B), or directly trigger transition (path C). Roughness-induced transition is relevant to path C. The set of parameters giving maximum transient growth factors is called optimal disturbances. The theory of transient growth and associated optimal disturbances has been intensively studied in the past (e.g., [14]) and more recently extended to compressible boundary layers by Tumin and Reshotko [15–17].

At the moment, the only method of industrial application, taking into account theoretically (although incompletely) the destabilizing mechanisms, is the modal linear stability theory (LST) [18], path A. Local or nonlocal [i.e., parabolized stability equations] theories may be applied. They both rely on the e^N method and are of comparable efficiency in predicting the point of transition; their difference for a given N may be of the same order of magnitude of the uncertainty on the value of N itself at the transition location. The real interest of nonlocal theories is to open the way for non linear theories that allow a deeper understanding of the transition processes. The strategy (i.e., the integration path) to compute the N factors is still not clearly defined, and this question will be addressed in the present study. However, $N \approx 10$ is a currently accepted value for the transition to occur in flight conditions. In wind tunnels, this value may be decreased dramatically [19].

The LST applies to mean-flow profiles and is very sensitive to their accurate description. In cases of flat plates or sharp cones at zero AOA, self-similar mean-flow profiles are available through the Levy–Lees and Mangler transformations. In case of a real-shape forebody, no such quasi-analytical solutions exist, and one has to use a CFD code to calculate the 3-D mean flow. Because strong shock waves are present in hypersonic flight conditions, robust solvers are needed. Until quite recently, wall-bounded flows were obtained by Euler/BL weak or strong coupling, but 3-D effects and flow separation were difficult to handle. Navier–Stokes solutions have already been obtained for stability calculations in the case of a small-scale ($L \approx 0.25$ m), axisymmetric model at ONERA (France) [20], allowing for very-well-resolved BL profiles (first cell $= 5$ μm). A previous study [21] has shown the feasibility of such calculations on a full-scale forebody with the FLUENT® industrial software. It was found very difficult, from a technical point of view, to properly extract the profiles from unstructured data. The impact of the numerical treatment of relatively low-resolution BL profiles (e.g., interpolation, derivation) on the subsequent stability calculations [performed with a code developed at Institut de Combustion, Aérothermique, Réactivité et Environnement (ICARE)] has been carefully examined and will be reported here. Nevertheless, two specific points are still to be addressed:

1) In the case of 2-D or axisymmetric geometries, the direction in which unstable waves are amplified is aligned with the mean flow. Hence, both the amplification direction and the integration path for the computation of N factors are clearly defined. This is no longer the case for a 3-D flow. How should these parameters be specified physically? Are the computed N values very dependent on these choices?

2) The blunt leading edge of the vehicle induces a bow shock and consequently an entropy layer (EL) that merges downstream with the BL. How does the EL modify the BL stability properties? More precisely, which part of the near-wall flow profiles should be retained for the stability analysis?

The present paper reports LST predictions on a full-scale forebody at a hypersonic flight Mach number for applied, industrial, transition prediction. Section II details the mean-flow calculation, with emphasis on the numerics, thermodynamic, and transport models. The topology of the flow is analyzed in reference to stability issues. Section III is devoted to the stability analysis theoretical framework. Previous studies on similar flow topologies are first reviewed in relation with the present configuration. The LST is briefly recalled, and items 1 and 2 are discussed. The sensitivity of the method to the grid resolution and to the thermodynamic and transport models will be discussed in Sec. IV. Finally, Sec. V gathers the stability results for the entire flow under the forebody and corresponding N factors for flight Mach numbers 4, 6, and 8. Comparison with the classical Re_θ/M^e correlation is done for completeness, and indications for future work are given as a conclusion.

II. Mean Flow

A. Flight Conditions and Thermodynamic and Transport Models

The considered hypersonic vehicle is supposed to fly from Mach 4 to Mach 8 at altitudes of 20 to 30 km. Static conditions in flight (taken from the 1976 U.S. Standard Atmosphere), freestream Mach number (outside BL + EL, AOA = 4 deg), and adiabatic wall conditions are gathered in Table 1.

In all calculations presented hereafter, air is a mixture of N_2, O_2, argon, and CO_2, as defined in Alexander Burcat and Ruscic's thermodynamics database [22]. It differs slightly from the U.S. Standard Atmosphere as reported in Table 2. Using Burcat and Ruscic's composition [22], the molar mass of air is $W_{\text{air}} = 28.96518$ kg/kmol.

Isobaric heat capacities of single components are given as coefficients of fourth-order polynomial fits for two ranges of temperature, 200–1000 K and 1000–6000 K. Because, at high altitude, static temperatures are in the low-range limit, only the high-temperature range is retained from Burcat and Ruscic [22]. At low temperatures, data from Lemmon et al. [23], which are accurate from 80 to 2000 K, are used instead for N_2 and O_2 (Lemmon et al. do not

Table 1 Flight conditions

M_∞	Altitude, km	P_∞, Pa	T_∞, K	M^e	T_w, K
4	20	5475	216.6	3.4–3.6	800–900
6	25	2512	221.6	4.2–5.0	1500–1650
8	30	1172	225.5	5.2–6.1	2500–2700

Table 2 Air composition, mole fractions

Component	Burcat and Ruscic[22]	U.S. Standard Atmosphere	Weight (kg/kmol)
N_2	0.780 840	0.780 840	28.013 48
O_2	0.209 476	0.209 476	31.998 80
Ar	0.009 365	0.009 340	39.948 00
CO_2	0.000 319	0.000 314	44.009 80
Total	1.000 000	0.999 970	——

provide any value for CO_2). The two curves are matched numerically at 1000 K. Then the heat capacity of the air is computed from single components' properties as a mole-weighted average for each temperature range. The resulting global fit is given in the Appendix (see Table A1 and Fig. A1).

The viscosity $\mu(T)$ of air is calculated with Wilke's mixing formula [24]

$$\mu = \sum_{\alpha=1}^{N_{sp}} \frac{X_\alpha \mu_\alpha}{\sum_{\beta=1}^{N_{sp}} X_\beta \phi_{\alpha\beta}}; \qquad \phi_{\alpha\beta} = \frac{(1 + \sqrt{\mu\alpha/\mu_\beta}(W_\beta/W_\alpha)^{\frac{1}{4}})^2}{\sqrt{8(1 + W_\alpha/W_\beta)}} \tag{1}$$

in which single component values $\mu_\alpha(T)$ are obtained from the CHEMKIN II [25] transport model based on the kinetic theory. The same method is applied for the thermal conductivity $k(T)$ of air, changing $\mu_\alpha(T)$ to $k_\alpha(T)$. Polynomial fits are applied to Eq. (1), of the fifth and third orders for μ and k, respectively (see Table A2 in the Appendix), accurate in the range 100–5000 K. The thermodynamic and transport models have been validated [21] on the classic $M^e = 10$ adiabatic flat plate of Malik and Anderson [26] (see Sec. IV).

B. Grid Requirements and Calculation Setup

The forebody is about 1.3 m long, with a cross section at the air inlet of about 0.5×0.2 m. It has a blunt nose of radius 5 mm. Upper and lower faces are plane, with angles +5 deg and −4 deg, respectively, with respect to the vehicle's X axis (see Fig. 5 for the definition of the vehicle reference frame). Figure 2 shows the computational mesh of the forebody lying on its back or upside down to make the area of interest visible. For meshing conveniences, a vertical cutting plane separates the nose region from the body region 0.04 m downstream from the nose tip. In the nose region, the mesh is hexahedral and unstructured (Fig. 3), and in the body region of interest for the LST calculations, the mesh is fully structured.

The grid convergence of the mean flow has been investigated by building different meshes, for which the parameters are gathered in Table 3. Meshes 1 to 4 are designed for $M_\infty = 6$ and 8, and mesh 5 for $M_\infty = 4$. In the latter case, the size of the computational domain has been increased to avoid numerical reflection of the shock wave on the external boundary. For each mesh, the height of the first cell is about 0.05 mm all along the body, which is enough to capture properly both the shock, as it can be seen in Fig. 4, and the BL. The sensitivity of mean-flow profiles and of the related eigenvalue on the grid resolution will be addressed in Sec. IV.

Calculations have been performed using the second-order upwind implicit density-based solver available in FLUENT 6.3.26, with Roe's flux. The CFL number is increased progressively from 0.1 to 1.5. The wall is considered as either adiabatic, or radiating with emissivity of $\sigma = 0.8$ in thermal equilibrium with the flow, which is

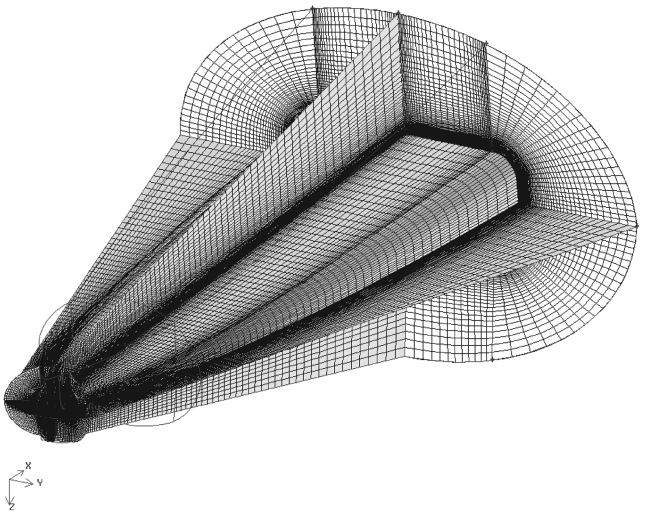

Fig. 2 Overview of the computational mesh.

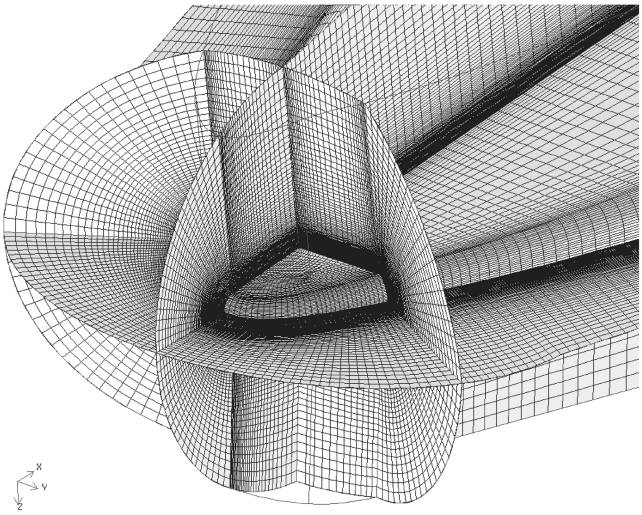

Fig. 3 Detail of the unstructured mesh of the nose region.

the most representative of flight conditions. Far-field nonreflecting characteristic-based boundary conditions are imposed. This boundary condition is not very accurate in the exit section, between the wall and the sonic line in the BL, but it affects only the last two rows of cells. Convergence is obtained after 15,000 iterations, taking about 50 h of CPU time on 4 Intel bi-Xeon 3.2 GHz (8 processors) for mesh 4. Convergence criteria are based on numerical residuals, on mass balance, and on wall temperature and skin friction in the plane of symmetry of the vehicle. All the results presented hereafter have been obtained with mesh 4 for $M_\infty = 6$ and 8, and with mesh 5 for $M_\infty = 4$.

C. Topology of the Flow

We consider here a flight at Mach 6 at an AOA of 4 deg, as an illustration. The contour of the Mach number is displayed in Fig. 5. The distance from the shock to the nose is about 2 mm. This implies very high thermal loads on the tip of the vehicle. Moreover, because the shock wave is closer to the lateral than to the upper or lower faces, a pressure gradient drives the near-wall flow from the edge toward the centerline of the vehicle. Figure 6 shows the streamlines computed from the first row of cells above the wall; they converge toward the plane of symmetry, and the near-wall flow rolls up into a pair of counter-rotating longitudinal vortices on both sides of the symmetry plane, as shown in Fig. 7. Two additional smaller vortices are also present very near the wall on the centerline, but not visible on the figure. Only mesh 4 is fine enough to capture properly these vortical structures. These vortices may be considered as a 3-D laminar separation. This region will be excluded from the stability analysis because the parallel flow assumption does not apply here.

The bluntness of the nose induces a bow shock and then an EL which is mostly visible as a loss in total pressure (Fig. 8). The EL combines with the longitudinal vortices near the plane of symmetry to produce velocity profiles of complicated shapes. Figures 9 and 10 show the streamwise and spanwise velocity profiles, respectively, at $X = 0.6$ m. The influence of the vortices is clearly visible at the first two locations ($Y = 0.01$ m, $Y = 0.013$ m); close to the vertical plane of symmetry, low-momentum flow coming from the near-wall region is pulled up (see Fig. 7, mushroomlike shape) and induces the

Table 3 Numbers of cells in the zone of interest (ZI) for different meshes

	Mesh 1	Mesh 2	Mesh 3	Mesh 4	Mesh 5
ZI: X	56	90	90	90	95
ZI: Y	32	32	40	60	72
ZI: Z	71	101	101	101	141
ZI: total	127,232	290,880	363,600	545,400	964,440
Total	9.0×10^5	1.7×10^6	2.0×10^6	2.0×10^6	3.3×10^6

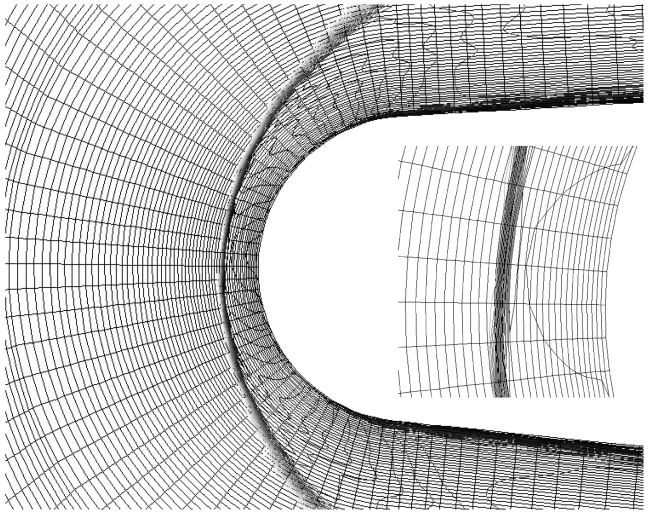

Fig. 4 Resolution of the shock in the plane of symmetry ($M_\infty = 6$, mesh 4).

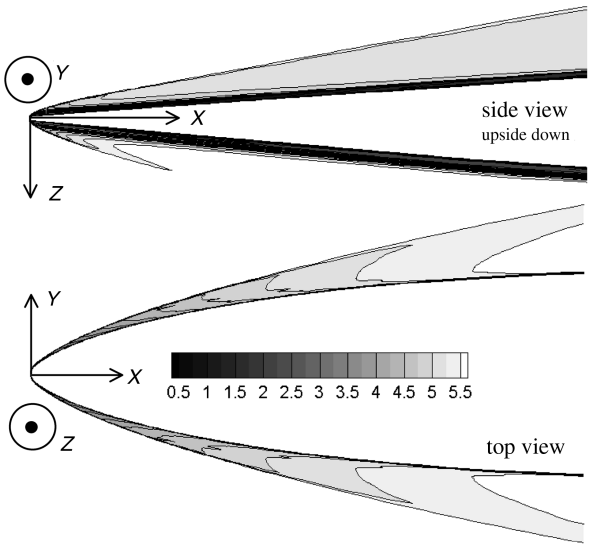

Fig. 5 Contour of Mach number ($M_\infty = 6$, AOA $= 4$ deg).

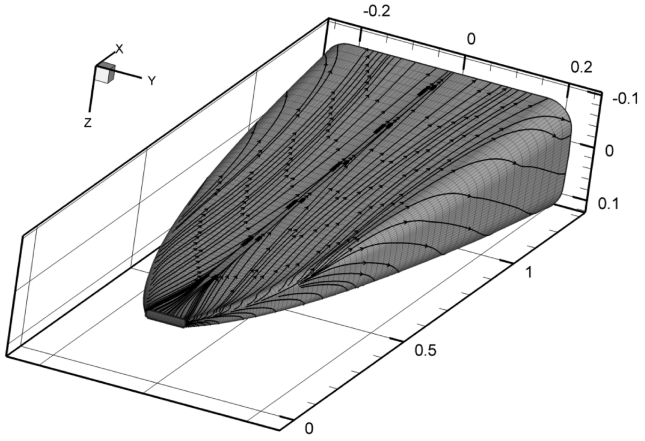

Fig. 6 Streamlines under the forebody ($M_\infty = 6$, AOA $= 4$ deg); axis units are meters.

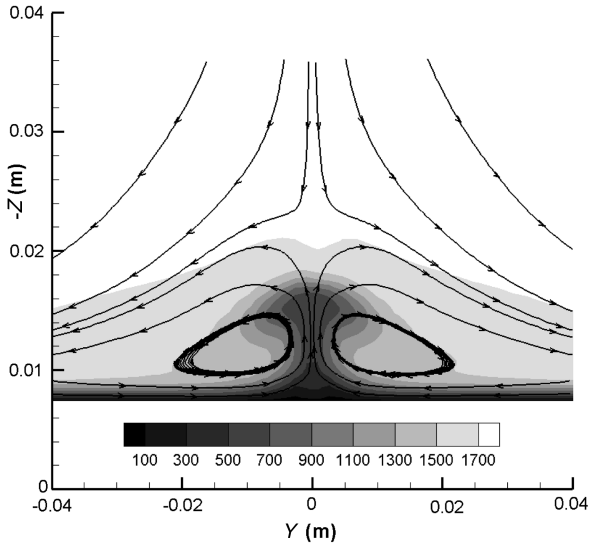

Fig. 7 Contour map of streamwise velocity (m/s) at $X = 0.5$ m; streamlines illustrate the longitudinal vortices.

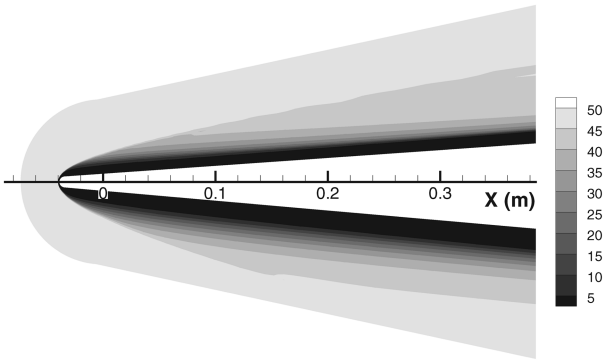

Fig. 8 Contour of total pressure (bars), side view, partial, and upside down, showing the EL in dark.

nonmonotonicity of the velocity profiles. From $Y = 0.017$ m to $Y = 0.05$ m, profiles exhibit a structure characteristic of a mixed boundary–entropy layer. At $Y = 0.07$ m, the EL almost disappears and a standard boundary-layer profile is recovered. In Sec. III.D, item 2, the influence of the EL on the stability results, will be discussed.

III. Stability Analysis

A. Modes: Terminology

In hypersonic flows, normal modes are classified as Mack's first and second (or higher) modes, crossflow (CF) instability, and entropy-layer instability. In fact, it has been shown by Fedorov and Khokhlov [27], Fedorov and Tumin [28], and Forgoston and Tumin [29] that second-mode instability is due to synchronization of the first and second mode, which consequently may be considered as a single mode: "...their frequency and phase speed coincide at some points" ([27] p. 361). Anyway, we will keep here the terminology "first" and "second" modes, which are well ingrained and understood in the field. The first mode is a 3-D mode for which the direction of propagation is oblique with respect to the mean-flow direction, whereas the second mode, which occurs for $M^e > 5$, is a 2-D mode. Crossflow modes are associated with the inflexional transverse (here spanwise) velocity component W (see Figs. 10 and 11). They are almost perpendicular to the mean-flow direction, and may possibly have a zero phase speed (stationary waves, $f = 0$ Hz). Nevertheless, their group velocity does not vanish, hence, they are convectively unstable.

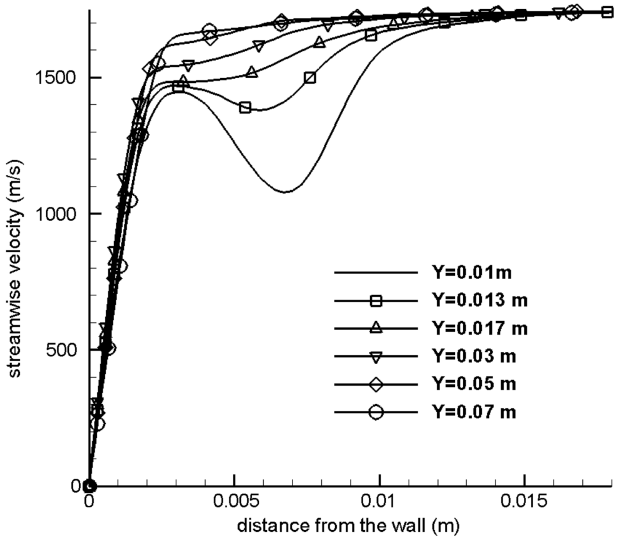

Fig. 9 Streamwise velocity profiles in the $X = 0.6$ m cross section.

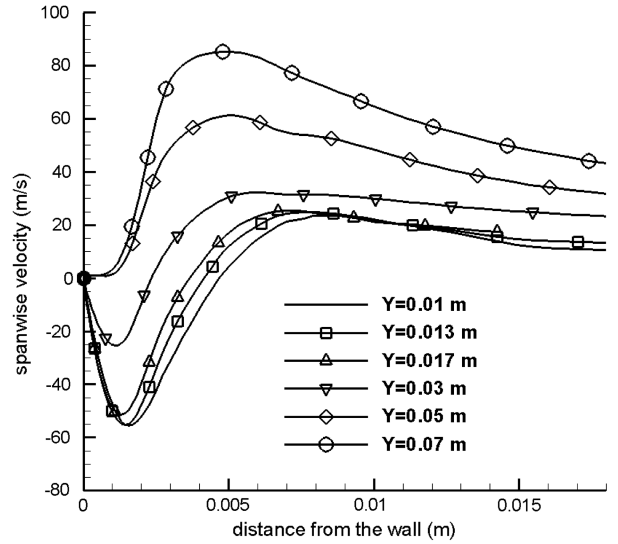

Fig. 10 Same as Fig. 9 for the spanwise velocity component.

B. Known Similar Configurations

1. *Existing Scramjet Forebodies*

Schneider [10] reports a limited number of studies on the stability of the flow under generic scramjet forebodies of the Hyper-X program, including the Hyper2000 and the X-43 A. These forebodies are mainly bidimensional and possess two compression corners (three compression ramps) ahead of the air inlet. Some instability mechanisms were put into light by these studies, including 1) first and/or second modes ahead of the first compression corner, 2) Kelvin–Helmholtz instabilities in the separated flow at the corners, 3) crossflow instability after the reattachment, on the second compression ramp, and 4) Görtler centrifugal instability near the corners.

Some possible interactions between vortices emanating from the nose tip and CF or Görtler instabilities were also highlighted [30]. These geometries noticeably differ from the present forebody. In particular, as it can be seen in Fig. 6, the forebody is three-dimensional with a flat surface and no compression corner. Therefore, Kelvin–Helmholtz and Görtler instabilities play no role in the transition mechanisms. On the other hand, we can expect first or second modes and CF waves.

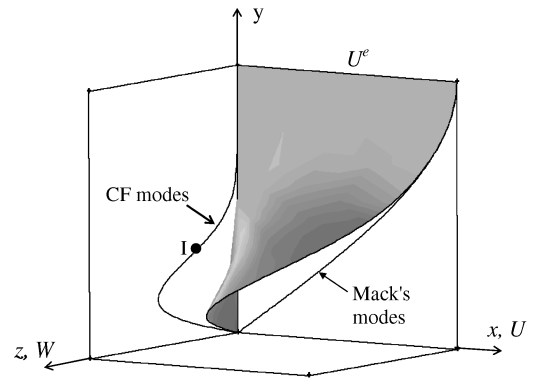

Fig. 11 Sketch of a 3-D mean flow and associated unstable modes.

2. *Sharp Cones at Angle Of Attack*

Numerical and experimental studies have been conducted at ONERA [31] on a 7 deg, 20 cm long, sharp cone at incidence 2 deg, Mach 7. Transition, detected using infrared imaging, varies from $x/L = 0.40$ on the leeward ray, $x/L = 0.61$ on the equator, and $x/L = 0.76$ on the windward ray. Calculations show that the transition is due to a combination of Mack's oblique first mode and crossflow instability, the former being predominant in the vertical plane of symmetry and the latter in the equatorial region. Schneider (Fig. 36 of [10]) reports similar observations on sharp circular cones at AOA: transition occurs earlier on the leeward ray, where the boundary layer is thicker.

3. *Sharp Elliptic Cones at 0 Degree Angle of Attack*

The present forebody has a common feature with the 0 deg AOA elliptical cone of Kimmel et al. (numerical [32], experimental [33]) for which the shock wave is closer to the major axis than to the minor axis. Hence, a pressure gradient causes crossflow from the attachment line located along the major axis, toward the vertical plane of symmetry (Fig. 6 of [32]). This accumulation leads to a thickening of the boundary layer and to a possible separation. Experiments show that transition occurs first on the minor axis line and then on rest of the surface. The LST for $M_\infty = 7.95$ and $Re_u = 3.3 \times 10^6/\text{m}$ confirms CF-dominated instability on the whole cone surface except near the symmetry planes where the flow is bidimensional. Early transition on the minor axis is due to inflexional, decelerated, boundary-layer velocity profiles generated by low-momentum fluid flow from the major axis.

4. *Bluntness and Entropy Layer*

Contrary to the preceding case, the present forebody has a blunt nose tip. It is well known [34] that the nose bluntness has an impact on the transition location; increasing the bluntness of an initially sharp cone first moves the transition downstream, then upstream with further increase. This reversal movement may be due to instabilities in the EL. Several mechanisms through which EL instabilities can actually promote transition have been proposed for blunted plates [35] or cones [36]. All these scenarios assume that the EL instabilities are too weak to trigger the transition by themselves. Nevertheless, Dietz and Hein [37] identified two types of EL instability: the first corresponds to weakly amplified waves with large propagation angles and the second is two-dimensional, linked to the maximum of $\rho\partial U/\rho\partial y$, with an amplification rate 1 order of magnitude higher than the former. The latter matches some experimental observations obtained by Brinich [38]. The bluntness effect on cones at AOA is reviewed by Schneider [10]. As for sharp cones, transition occurs earlier on the leeward ray than on the windward ray, except for the largest nose radius (Fig. 37 of [10]). Schneider explains this exception, indicating that some nosetip-roughness-related mechanisms are more likely to occur for larger nose radii.

C. Stability Theory and the e^N Method: Item 1

The LST is well known. Equations are recalled here to introduce notations, mainly those related specifically to item 1, mentioned in the introduction.

First, a coordinate system attached to the wall (and not to the streamlines at the outer edge of the BL) is defined. Because the wall is a plane, this coordinate system is the same for the whole surface: x is lying along the wall in the $\{X, Z\}$ plane, y is the distance to the wall, and $z = -Y$ is the transverse direction. Corresponding unit vectors are $\boldsymbol{x}$, $\boldsymbol{y}$, and $\boldsymbol{z}$.

In the 3-D compressible Navier–Stokes equations, the mean-flow variables $\{\rho, U, V, W, P, T\}$ are perturbed by normal modes of the form

$$q'(x, y, z, t) = \hat{q}(y) \exp[i(\alpha x + \beta z - \omega t)] \tag{2}$$

The parameters α, β, and ω can either be real or complex, according to the nature of instabilities. Here, instabilities are convective, so the spatial approach is adopted. Wave numbers $\alpha = \alpha_r + i\alpha_i$ and $\beta = \beta_r + i\beta_i$ are complex, and the pulsation $\omega = 2\pi f$ is real. Hence, perturbations become

$$q'(x, y, z, t) = \hat{q}(y) \exp(-\alpha_i x - \beta_i z) \exp[i(\alpha_r x + \beta_r z - \omega t)] \tag{3}$$

Fluid properties $\{C_p, C_v, \mu, k\}$ are also perturbed as, for example

$$C'_p = \left(\frac{\mathrm{d}C_p}{\mathrm{d}T}\right) T'$$

The stability solver developed at ICARE uses the fully variable thermodynamic and transport models previously described in Sec. II.A.

A 3-D perturbation of given frequency f is characterized by the wave vector $\boldsymbol{k} = \alpha_r \boldsymbol{x} + \beta_r \boldsymbol{z}$ and propagates in the direction

$$\psi = \tan^{-1}\left(\frac{\beta_r}{\alpha_r}\right) \tag{4}$$

with the phase velocity

$$V_\varphi = \frac{\omega}{|\boldsymbol{k}|} = \frac{\omega}{\sqrt{\alpha_r^2 + \beta_r^2}} \tag{5}$$

Its amplitude

$$A(x, z) = |\hat{q}(y)| \exp(-\alpha_i x - \beta_i z) \tag{6}$$

is growing (or decreasing) with the rates

$$\frac{1}{A}\frac{\partial A}{\partial x} = -\alpha_i \quad \text{in the } x \text{ direction} \tag{7}$$

$$\frac{1}{A}\frac{\partial A}{\partial z} = -\beta_i \quad \text{in the } z \text{ direction} \tag{8}$$

which define an amplification vector $\boldsymbol{\sigma} = -\alpha_i \boldsymbol{x} - \beta_i \boldsymbol{z}$ and a growth direction

$$\bar{\psi} = \tan^{-1}\left(\frac{\beta_i}{\alpha_i}\right) \tag{9}$$

Perturbed equations are linearized (quadratic perturbation terms are neglected) and the mean flow is assumed to be parallel $V = 0$. This is the local LST framework. The resulting set of differential equations for the amplitude of perturbations (normal mode equations for the eigenfunctions of the fluctuations) is given by Mack [8]. These equations are integrated from the outer edge of the BL, where mean-flow gradients are negligible, down to the wall, using a fourth-order Runge–Kutta scheme and a Gram–Schmidt orthonormalization procedure. From known vanishing boundary conditions in the freestream, the eigenvalues $\{\alpha, \beta, \omega\}$ of the problem are to be found using a shooting/Newton–Raphson procedure in order to satisfy the wall boundary condition $\hat{v}(y = 0) = 0$. The other wall boundary conditions are imposed ($\hat{u}(0) = \hat{w}(0) = \hat{T}(0) = 0$), and the pressure fluctuation may be chosen arbitrarily ($\hat{p}(0) = 1$). At convergence, the eigenvalues are related through the (numerically obtained) dispersion relation:

$$\mathcal{D}(\alpha, \beta, \omega) = 0 \tag{10}$$

However, a problem remains in the fact that Eq. (10) is not a closed relation in the spatial theory, and the value of β_i is undetermined and must be somewhat fixed or computed. The problem may be reported on the growth direction $\bar{\psi}$. Several approaches have been proposed [19]. In 2-D flows, it is assumed that the amplification is aligned with the mean flow ($\beta_i = \bar{\psi} = 0$). In 3-D flows, there are classically three options:

1) Use an additional relation to compute β_i [39,40].

2) Impose, as in 2-D flows, the value of β_i (e.g., $\beta_i = 0$). This approach has been proposed by Mack [41] for swept wings.

3) Assume the direction of amplification $\bar{\psi}$. There are two usual choices:

a) $\bar{\psi} = \theta_g$, where θ_g is the local direction of the real group velocity. This option is physically justified by the fact that, in a conservative media, the energy of a wave packet travels with its group velocity.

b) $\bar{\psi} = \arctan(W^e/U^e)$, which avoids the calculation of the group velocity and may be justified by the observation that θ_g is approximately the local direction of the flow outside of the BL [19]. The outer edge of the BL + EL is fixed just below the shock.

Solution 1 is difficult to apply in the present industrial context, and solution 2 is only relevant to the case of swept wings, in a reference frame attached to the leading edge. Solutions 3a and 3b will be tested and compared with solution 2 in Sec. III.E. Solution 3a needs the calculation of the real group velocity, or at least its direction. Although we noticed that Eq. (10) does not depend much on $\bar{\psi}$ or β_i, especially when $\bar{\psi} < 20$ deg which is the case in all calculations presented in Sec. V, the determination of the group velocity is, however, important to define the integration path for the computation of N factors. In the general case, the group velocity is a complex vector

$$\boldsymbol{V_g} = \frac{\partial \omega}{\partial \alpha}\boldsymbol{x} + \frac{\partial \omega}{\partial \beta}\boldsymbol{z} \tag{11}$$

for which the real part

$$\Re\{\boldsymbol{V_g}\} = \frac{\partial \omega_r}{\partial \alpha_r}\boldsymbol{x} + \frac{\partial \omega_r}{\partial \beta_r}\boldsymbol{z} \tag{12}$$

is evaluated, most of the time, in the temporal approach because, in that case, α and β are real and fixed and the calculation is straightforward (by approximating differentials by small differences). The direction θ_g of $\Re\{\boldsymbol{V_g}\}$ is apparent and the spatial stability calculation is further performed to get α_i using $\beta_i = \alpha_i \tan\theta_g$. That means two successive stability calculations.

An original alternative method is now proposed to compute directly θ_g (but not $\Re\{\boldsymbol{V_g}\}$) in the spatial approach where $\omega = \omega_r$, avoiding thus the additional temporal calculation. The direction θ_g of $\Re\{\boldsymbol{V_g}\}$ is defined by

$$\tan\theta_g = \frac{(\partial\omega_r/\partial\beta_r)_{\alpha_r}}{(\partial\omega_r/\partial\alpha_r)_{\beta_r}} = -\left(\frac{\partial\alpha_r}{\partial\beta_r}\right)_{\omega_r} \tag{13}$$

The relation of dispersion in Eq. (10) can be written as

$$\alpha = \alpha_r + i\alpha_i = \mathcal{D}_\beta(\beta_r, \beta_i, \omega) \tag{14}$$

or alternatively

$$\alpha = \alpha_r + i\alpha_i = \mathcal{D}_\psi(\psi, \bar{\psi}, \omega) \tag{15}$$

Depending on whether the form in Eq. (14) or Eq. (15) is used, $\mathrm{d}\alpha_r$ can be expressed by

$$\mathrm{d}\alpha_r = \left(\frac{\partial \alpha_r}{\partial \beta_r}\right)_{\beta_i,\omega} \mathrm{d}\beta_r + \left(\frac{\partial \alpha_r}{\partial \beta_i}\right)_{\beta_r,\omega} \mathrm{d}\beta_i + \left(\frac{\partial \alpha_r}{\partial \omega}\right)_{\beta_r,\beta_i} \mathrm{d}\omega \quad (16)$$

or

$$\mathrm{d}\alpha_r = \left(\frac{\partial \alpha_r}{\partial \psi}\right)_{\bar{\psi},\omega} \mathrm{d}\psi + \left(\frac{\partial \alpha_r}{\partial \bar{\psi}}\right)_{\psi,\omega} \mathrm{d}\bar{\psi} + \left(\frac{\partial \alpha_r}{\partial \omega}\right)_{\psi,\bar{\psi}} \mathrm{d}\omega \quad (17)$$

From Eqs. (4) and (9), $d\psi$ and $d\bar{\psi}$ car be calculated analytically, for example

$$\mathrm{d}\psi = \frac{\alpha_r}{\alpha_r^2 + \beta_r^2}\,\mathrm{d}\beta_r - \frac{\beta_r}{\alpha_r^2 + \beta_r^2}\,\mathrm{d}\alpha_r \gamma \quad (18)$$

and substituted into Eq. (17). Identifying the results with Eq. (16), an expression comes out for

$$\left(\frac{\partial \alpha_r}{\partial \beta_r}\right)_{\omega}$$

to be used in Eq. (13)

$$\theta_g = -\tan^{-1}\left(\frac{\left(\frac{\partial \alpha_r}{\partial \psi}\right)_{\bar{\psi},\omega} \frac{\alpha_r}{\alpha_r^2+\beta_r^2}}{1 + \left(\frac{\partial \alpha_r}{\partial \psi}\right)_{\bar{\psi},\omega} \frac{\beta_r}{\alpha_r^2+\beta_r^2}}\right) \quad (19)$$

The method has been validated on the 2-D Korteweg–de Vries equation and applied to get the results of the present study. In this method, the variations in ψ needed to estimate numerically $\partial\alpha_r/\partial\psi$ in Eq (19) is part of the envelope method discussed in the next section and does not introduce any additional computational effort.

D. Effect of the Entropy Layer: Item 2

1. Wall Thermal Conditions and Generalized Inflexion Points

Let's take the example of a typical flight at $M_\infty = 6$ (see Table 1), AOA = 4 deg, with either an adiabatic (hot) or radiating (cold) wall. Let's consider the location $\{\, x = 0.6 \text{ m}, \quad z = 0.017 \text{ m} \,\}$ close to the plane of symmetry. The longitudinal component $U(y)$ of the velocity profile has, in both cases, an inflexion point due to the entropy layer (Figs. 9 and 12). In fact, more relevant to the LST in compressible flows is the existence of a generalized inflexion point (GIP) at the altitude y_s where

$$\frac{\partial}{\partial y}\left(\rho \frac{\partial U}{\partial y}\right)\bigg|_{y_s} = 0 \quad (20)$$

The 2-D inviscid temporal theory of Lees and Lin [6] says that if such a GIP exists, a necessary and sufficient condition for the existence of a neutral wave is

$$\frac{U(y_s)}{U^e} > 1 - \frac{1}{M^e} \quad (21)$$

and the phase velocity of this neutral wave is $V_\varphi = U(y_s)$. The condition in Eq. (21) is moreover sufficient for the existence of an unstable wave. The quantity $\rho\partial U/\partial y$ is plotted in Fig. 13 for the profiles of Fig. 12. The total number of GIPs is 2 (respectively 3) in the radiating (respectively adiabatic) case. At the location considered, the freestream Mach number is $M^e = 4.92$ and the altitude y_0 where

$$\frac{U(y_0)}{U^e} = 1 - \frac{1}{M^e} = 0.796 \quad (22)$$

is 1.79 mm (respectively 2.37 mm) in the radiating (respectively adiabatic) case. Hence, the condition in Eq. (21) is satisfied by two GIPs for both the cold and hot walls, located at $y_s = 3.15$ and 7.13 mm (R1, R2, radiating), and $y_s = 5.43$ and 9.01 mm (A1, A2, adiabatic). If the stability analysis is performed for truncated base-flow profiles, for example cut at the edge y_c (not always clearly defined) of the boundary layer as shown in Fig. 12, results may be

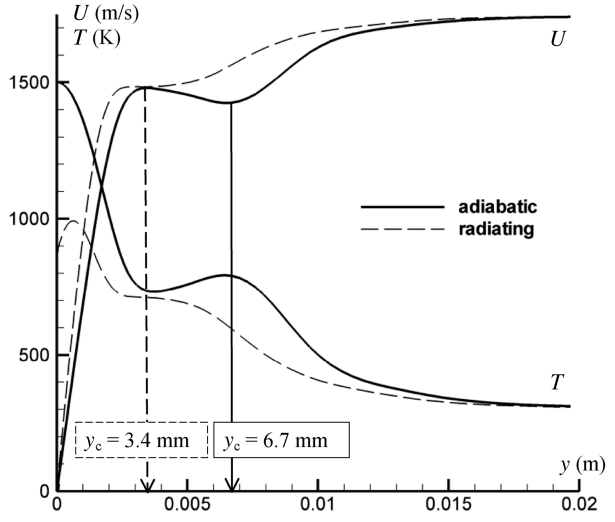

Fig. 12 Temperature and x-velocity profiles at $x = 0.6$ m and $z = 0.017$ m ($M_\infty = 6$, AOA = 4 deg).

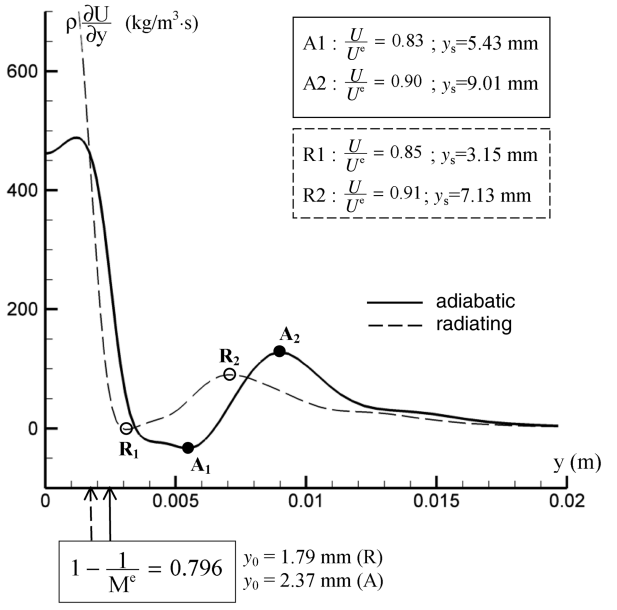

Fig. 13 Same conditions as Fig. 12 for generalized inflexion points.

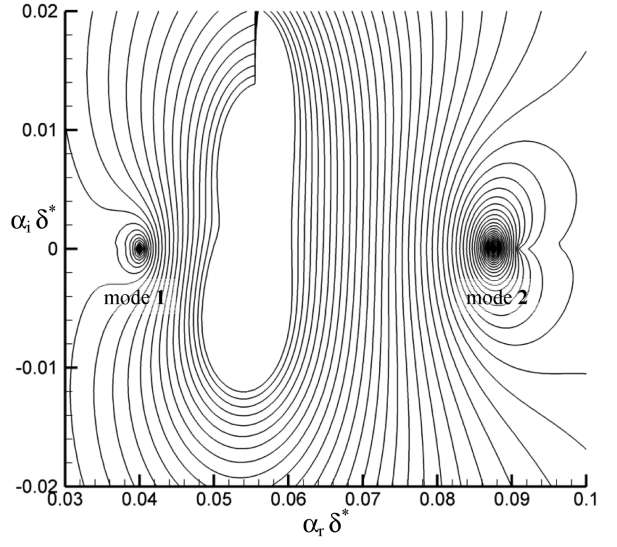

Fig. 14 Stability spectrum for profiles of Fig. 12, BL only (y_c cut) with the adiabatic wall ($f = 10$ kHz, $\psi = 0$ deg, $\delta^* = 1.26$ mm).

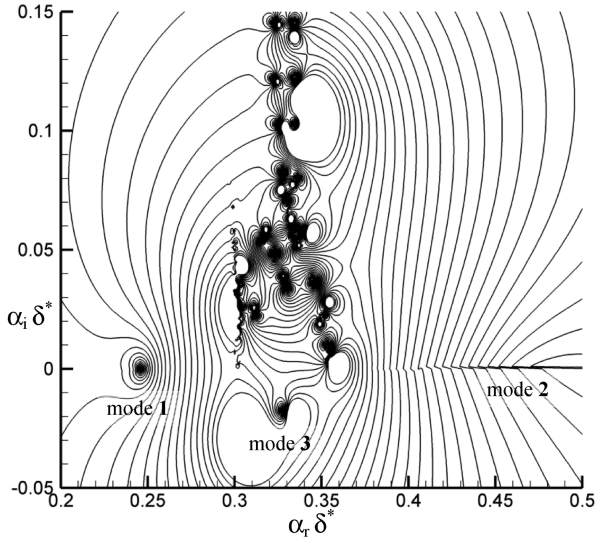

Fig. 15 Same as Fig. 14 for BL + EL ($\delta^* = 8.18$ mm).

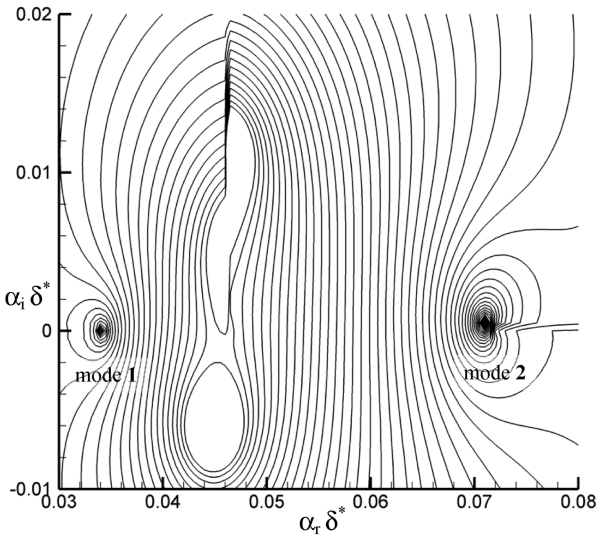

Fig. 16 Same as Fig. 14 for the radiating wall ($\delta^* = 1.09$ mm).

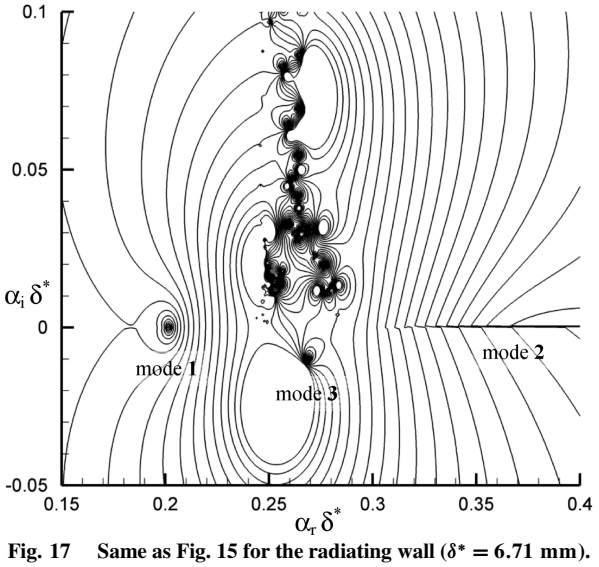

Fig. 17 Same as Fig. 15 for the radiating wall ($\delta^* = 6.71$ mm).

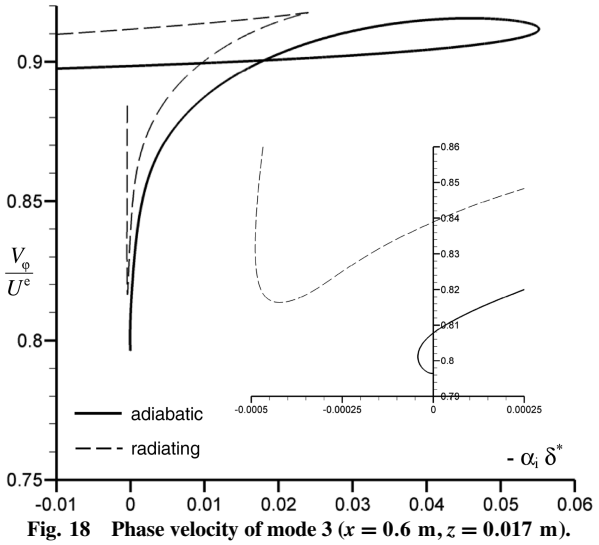

Fig. 18 Phase velocity of mode 3 ($x = 0.6$ m, $z = 0.017$ m).

incomplete. Notice that the choice of the altitude retained influences directly U^e and M^e and also the computed displacement thickness δ^*. A fast way to identify regions in the $\{\alpha_r, \alpha_i\}$ plane where solutions may be found is to plot the values of $\hat{v}(y = 0)$ obtained for a given $\{\omega, \psi, \bar{\psi}\}$ after a single Runge–Kutta integration procedure. This is done on Figs. 14–17 for the BL only and entire profiles (BL + EL) in each case, for $f = 10$ kHz and $\psi = \bar{\psi} = 0$ deg. Isolevels are distributed exponentially, so that low levels cluster in dark regions on the maps around the numerical solutions of the dispersion relation in Eq. (10) of the flow. Mode 1 is nonphysical ($V_\varphi > U^e$). Mode 2 is either a Mack's oblique first mode (linked to the streamwise velocity profile instability) or a crossflow (spanwise) instability, depending on the wall thermal condition and location on the forebody. Here, it is almost stable for $\psi = 0$ deg, but very unstable for $\psi \approx 85$ deg. This mode plays the major role in the transition process away from the plane of symmetry and will be intensively studied in Sec. V. At a higher Mach number ($M_\infty = 8$), an additional acoustic Mack's second mode is also present, because $M^e > 5$ (Table 1).

The obvious features on Figs. 15 and 17 are the large number of stable solutions that did not exist on Figs. 14 and 16, plus an additional unstable solution, called mode 3. The cloud of stable solutions should relate to Mack's discrete spectrum. Indeed, the number of modes is increased when the EL is taken into account, and mode 2 degenerates keeping $\psi = 0$ deg. Figure 18 shows the dimensionless phase velocity V_φ/U^e of mode 3 plotted against the opposite of the dimensionless amplification rate $-\alpha_i \delta^*$ for frequencies varying from 100 Hz to 120 kHz. The neutral curve is cut twice in each wall condition, at $V_\varphi/U^e \approx 0.81$ and 0.90 (adiabatic wall) and $V_\varphi/U^e \approx 0.84$ and 0.91 (radiating wall), in good accordance with the predictions of Lees and Lin's theory [6] (Fig. 13). This makes evident the relation between mode 3 and the GIPs, and tends to indicate an EL instability equivalent to that found by Dietz and Hein [37] on a blunted plate. Away from the vertical plane of symmetry, the EL vanishes (see Fig. 9) and only modes 1 and 2 remain.

2. *Local Properties of the Entropy-Layer Unstable Mode 3*

The mean flow studied by Dietz and Hein [37] is 2-D ($W = 0$). They found two EL unstable modes: the first is of low frequency and mostly amplified for $\psi \approx 90$ deg, the second is a 2-D wave ($\psi = 0$ deg) of higher frequency, an order of magnitude more amplified than the former. In the present case, the mean flow is 3-D. The dimensionless amplification factor $-\alpha_i \delta^*$ of the EL mode 3 is shown in Fig. 19 both for the 3-D mean-flow profiles (adiabatic and radiating wall) and for the same profiles with the z component W artificially set to 0. In all the cases, the amplification varies with the wave angle ψ, but the variations are small in the range [−45 deg, + 45 deg], before the mode becomes suddenly stable at about ±80 deg. The symmetry of the α_i distribution is lost when W is taken into account, which highlights some effects of the

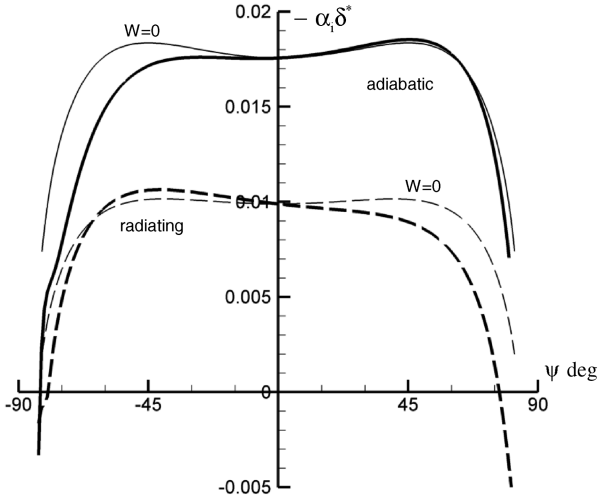

Fig. 19 Amplification rate of mode 3 as a function of the wave angle ($x = 0.6$ m, $z = 0.017$ m, $f = 10$ kHz, $\bar{\psi} = \beta_i = 0$).

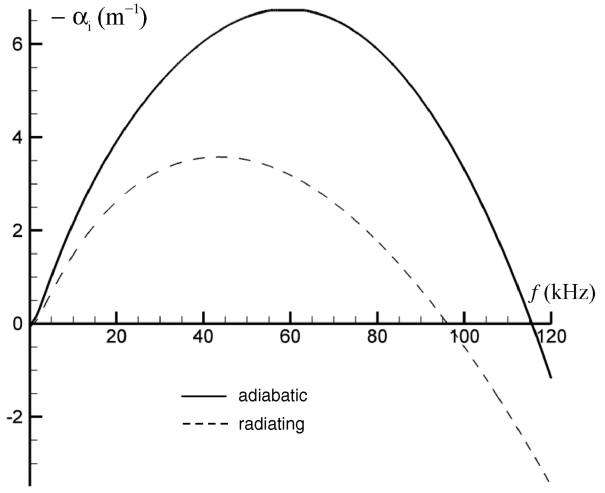

Fig. 20 Amplification rate of mode 3 as a function of the frequency ($x = 0.6$ m, $z = 0.017$ m, $\psi = \bar{\psi} = \beta_i = 0$).

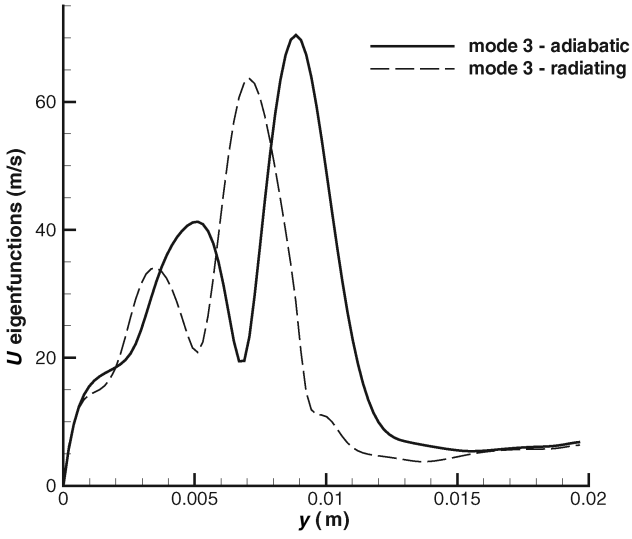

Fig. 21 Streamwise velocity eigenfunctions of mode 3 (adiabatic and radiating walls).

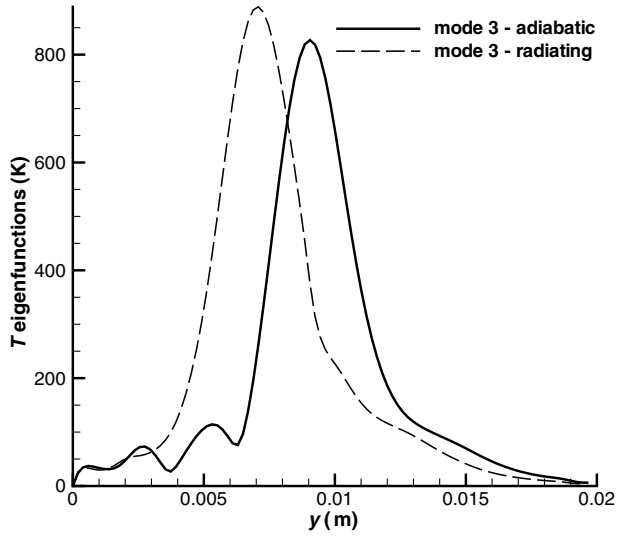

Fig. 22 Same as Fig. 21 for temperature eigenfunctions.

three-dimensionality of the flow on mode 3. However, these effects are weak. We can conclude that the entropy-layer instability found here is basically 2-D, of the same nature as the second mode of Dietz and Hein [37], and Fig. 20 shows that unstable frequencies of mode 3 range between a few kilohertz and almost 100 kHz.

The spatial structure of mode 3 can be observed on the x-velocity and temperature eigenfunctions. Figures 21 and 22 show that the EL instability is dominated by temperature fluctuations, once again in accordance with the second EL mode of Dietz and Hein [37]. The ratio $|\hat{T}|_{\max}/T_{\max}$ is approximately 0.6 (0.9) for the adiabatic (radiating) wall, whereas $|\hat{U}|_{\max}/U_{\max}$ is only 0.04 in both wall thermal conditions. The extrema of the eigenfunctions are located at the altitude of GIPs of Fig. 13. For comparison, eigenfunctions of mode 2 are also presented on Figs. 23 and 24, for $\psi = 0$ deg and $\psi = 65$ deg.

E. Integration Path in the e^N Method

In the e^N method, amplification rates of every unstable frequency are integrated along a path to be defined on the surface of interest (here the forebody of the vehicle). In compressible or 3-D flows, one possibility is to seek at each location, for a given frequency, the angle ψ_M for which the wave is mostly amplified. This is the so-called envelope method. Therefore, from Eq. (6), N factors are given by

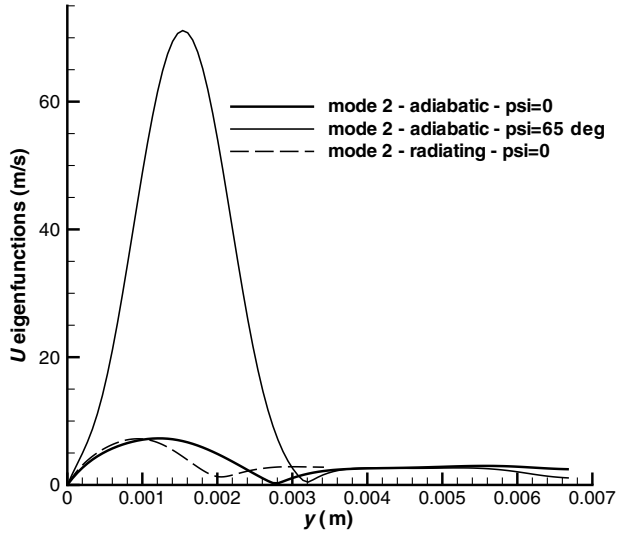

Fig. 23 Streamwise velocity eigenfunctions of mode 2 (adiabatic and radiating walls).

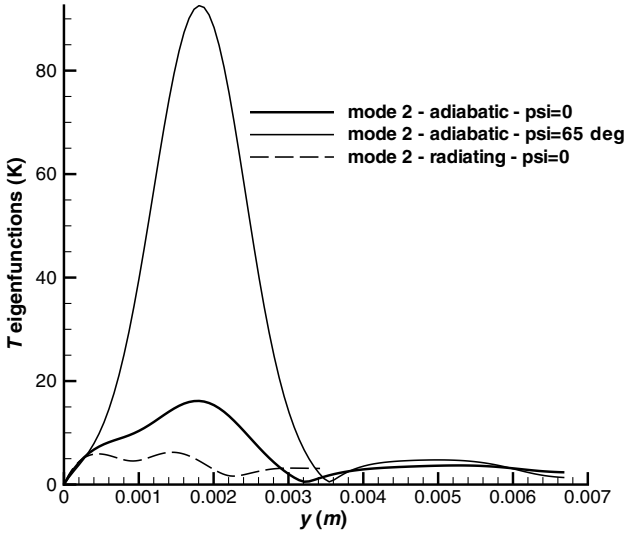

Fig. 24 Same as Fig. 23 for temperature eigenfunctions.

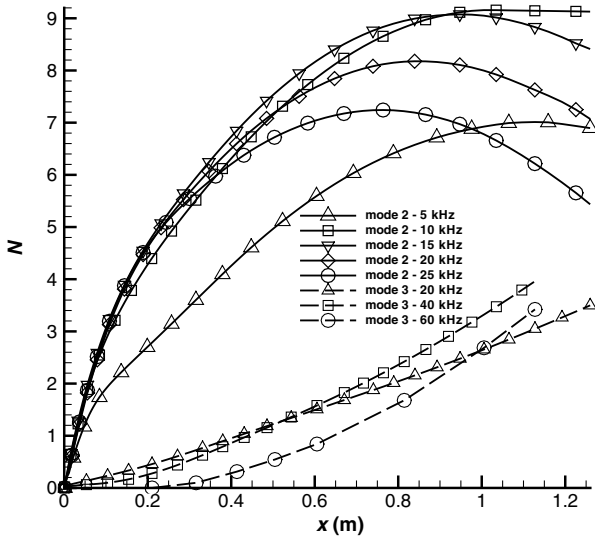

Fig. 26 N factors of the entropy layer mode 3 ($f = 20$, 40, 60 kHz, $\psi = 0$ deg) and of the crossflow mode 2 ($f = 10$ kHz, envelope method).

$$N(s,f) = \ell_n(A/A_0) = \max_{\psi} \int_{s_0}^{s} \sqrt{\alpha_i^2 + \beta_i^2}\, \mathrm{d}\xi \qquad (23)$$

where s_0 is the point on the path where the wave of amplitude A_0 at this location becomes unstable. The transition location is then determined using the upper-bound curve of all unstable frequencies.

The choice of the integration path in Eq. (23) should be coherent with the method used to compute β_i; the local tangent to the path must be the local angle $\bar{\psi}$ of amplification. This has some influence on the resulting N factors computed in approaches 2, 3a, and 3b in Sec. III.C, as illustrated hereafter. In the case $M_\infty = 6$ with AOA = 4 deg with a radiating wall, the N factors of mode 2 for the frequency $f = 10$ kHz using the envelope method for ψ are shown in Fig. 25. Black lines indicate the integration paths. Method 2 produces the lowest value of the N factor $N_{\max} \approx 6$, whereas method 3a gives $N_{\max} \approx 8.4$ and method 3b offers $N_{\max} \approx 8.6$. All these values are too weak for a natural transition in flight. However, in a noisy environment or at lower Mach number, they should provide sensibly different transition locations. Methods 3a and 3b produce similar maximum values, but the shape of iso-N contours is different.

For the sake of completeness, N factors of mode 3 (radiating case) have been computed for frequencies $f = 40$, 50, and 60 kHz and for $\psi = 0$ deg, on the whole length of the forebody, along the longitudinal mesh line close to the vertical plane of symmetry, crossing the point ($x = 0.6$ m, $z = 0.017$ m). For comparison, N factors of mode 2 have also been computed for several frequencies, using the envelope method ($\psi_M \approx 87$–89 deg, crossflow instability) along a mesh line lying at equal distance from the centerline and the edge of the body (this not any of the previously referenced methods, but close to 3b). These lines have been selected because they give the maximum total amplification for each mode. Figure 26 shows that mode 3 gives N factors of about 4, which is not enough to provoke a natural transition in flight. This is not in contradiction with the results of Kimmel et al. [33] on an elliptic cone (see Sec. III.B), for which transition occurred first on the centerline, because these results were obtained in a wind-tunnel for which N factors at transition are much smaller than expected in flight. As little is known so far about transition due to entropy-layer instability, further investigations are needed, both experimentally and numerically. Hence, results presented in Sec. V only refer to mode 2 and to the frequency $f = 10$ kHz, which has been found to be approximately the most amplified in all of the flight conditions that have been considered.

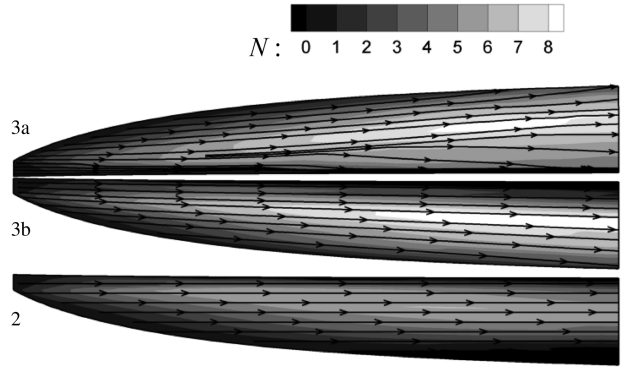

Fig. 25 Effect of LST strategy on the N factors ($M_\infty = 6$, AOA = 4 deg, $f = 10$ kHz, envelope method, radiating wall).

IV. Validation of the Method

A. Thermodynamic and Transport Model

To validate the thermodynamic and transport models and to check the impact of the perfect gas assumption, the classic $M^e = 10$ adiabatic flat plate of Malik and Anderson [26] is simulated. In the freestream, the static temperature is $T^e = 350$ K and the unit Reynolds number is $Re_u = 6.6 \times 10^6$ m^{-1}. In such high enthalpy flow, real gas effects become nonnegligible due to the dissociation of O_2 above 2500 K (N_2 above 4000 K). However, thermal equilibrium still holds (a single temperature exists: $T = T_{\text{trans}} = T_{\text{rot}} = T_{\text{vib}}$), although chemistry may be considered as infinitely fast (equilibrium) or having a finite rate (nonequilibrium). Malik and Anderson solved numerically the boundary-layer equations for the basic flow and considered three thermochemical models: 1) IG (ideal gas or calorically perfect), $\mathrm{d}h = C_p \mathrm{d}T$, $p = \rho r T$, with no chemical reactions, 2) PG (perfect gas or thermally perfect), $\mathrm{d}h = C_p(T)\mathrm{d}T$, $p = \rho r T$, with no chemical reactions, and 3) RGeq (real gas), $h = h(p,T)$, $p = \chi \rho r T$, involving equilibrium chemistry for dissociation of molecules.

This test case has also been calculated at ONERA by Perraud et al [31] with the code CASTHY, for nonequilibrium chemistry (referred to as RGneq), the basic flow being also computed from BL equations. In the present study, we use self-similar Levy–Lees solutions for the basic flow, with 1000 grid points a the BL. The pressure p^e is adjusted to match the value of Re_u.

Figure 27 shows the local reduced amplification rate $\alpha_i^* = \alpha_i \sqrt{x\nu^e/U^e}$ of unstable frequencies at $x = 0.61$ m ($\sqrt{Re_x} = 2000$) as a function of the reduced frequency $F = 2\pi f \nu^e / U^{e2}$. Results show that three modes of instability are present. The first is the classical Mack's oblique first mode with the variable ψ_M. Its amplification rate is computed with the envelope method. The second is Mack's 2-D ($\psi_M = 0$ deg) acoustic mode, the peak

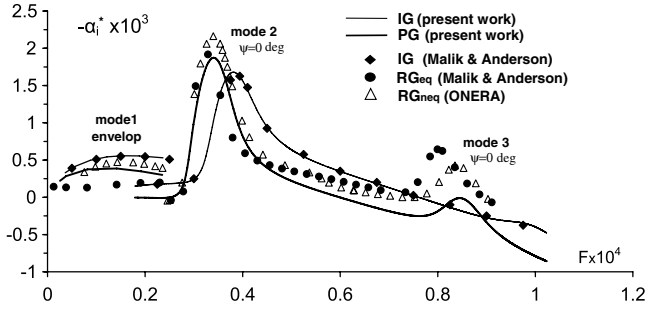

Fig. 27 Amplification rates ($M = 10$ adiabatic flat plate, $\sqrt{Re_x} = 2000$).

occurring at $f \approx 130$ kHz. The third mode (not to be confused with EL mode 3 of Sec. III.D) is found at $f \approx 315$ kHz, a frequency so high that it is unlikely to occur in the context of the present study.

The IG model cannot reproduce the physics associated with the third mode, as already found by Malik and Anderson [26]. The PG model hardly detects this high-frequency mode but is surprisingly in better agreement with RGneq than with RGeq concerning the first mode. The second mode is globally well captured with the PG model, the differences between RGeq and RGneq being quite small. In this severe test case, wall temperatures found by Malik and Anderson are $T_{w,\mathrm{IG}} \approx 6125$ K and $T_{w,\mathrm{RGeq}} \approx 3150$ K. Perraud et al. [31] have found $T_{w,\mathrm{RGeq}} \approx 3100$ K and $T_{w,\mathrm{RGneq}} \approx 4800$ K. With the present model, $T_{w,\mathrm{PG}} \approx 4984$ K is obtained. For the vehicle in flight at $M_\infty = 8$, the highest wall temperature computed is about 2700 K (adiabatic wall, Table 1). Hence, the thermodynamic and transport model of Sec. II.A is highly reliable for the purposes of the present study.

B. Flat-Plate Calibrations

The numerical integration of LST ordinary differential equations described in Sec. III.C needs about 1000 grid points across the BL to be stable and accurate. This it not possible in a full-scale, 3-D Navier–Stokes calculation, as the total number of grid points would be prohibitive. Hence, the numerical procedure adopted is as follows:

1) Compute the basic flow with the FLUENT code with a few tens of grid points in the BL + EL. The finite-volume scheme provides cell averages, so extrapolate the wall temperature at the third order from the three neighboring cells.

2) In the stability code, compute first and second derivatives of the mean-flow profiles with second order finite-differences.

3) Interpolate these values on 1000 points to run the stability calculations.

Results presented hereafter compare adiabatic flat-plate Levy–Lees (L–L) self-similar solutions to Navier–Stokes (N–S) BL profiles. The freestream conditions are $M^e = 2.68$, $T^e = 752$ K, and $p^e = 4640$ Pa, representative of a flight at $M_\infty = 6$, altitude 25 km. The flat plate is 6 m long, and the BL thickness at the end is about 20 mm. In the N–S calculations (step 1), the rectangular computational domain is 6×1 m. The BL region is described with 50 regular cells of 0.52 mm height (total height is 26 mm), and then the mesh is stretched to reach freestream conditions 1 m above the wall with 100 additional cells. The reference case is L–L with 1000 points and accurate derivation and no interpolation.

Figures 28 and 29 show mean-flow profiles and their second derivatives, respectively, at $x = 1$ m from the leading edge. Less than 25 cells are present in the BL at this location. Although the profiles themselves compare very well, the consequences of their numerical treatment (steps 2 and 3) can be observed by comparison of the N–S calculation to a calculation where 50 points are retained in the L–L solution before derivation and interpolation and to the

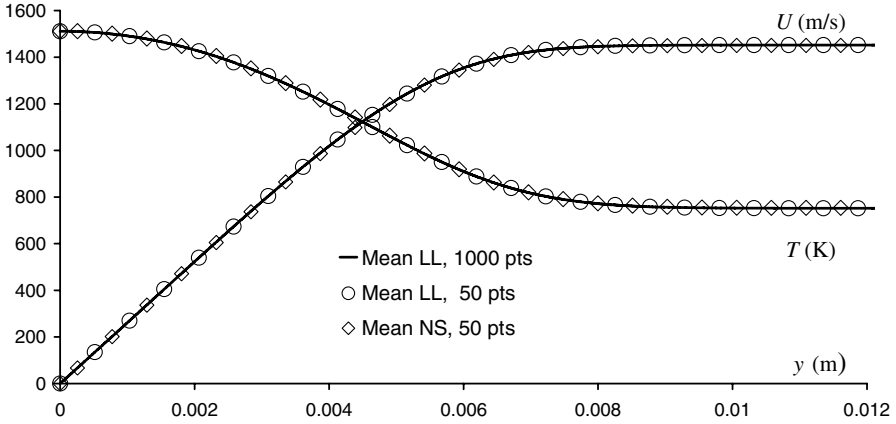

Fig. 28 Adiabatic flat plate ($M^e = 2.68$, $T^e = 752$ K, $p^e = 4640$ Pa) with mean-flow velocity and temperature profiles at ($x = 1$ m).

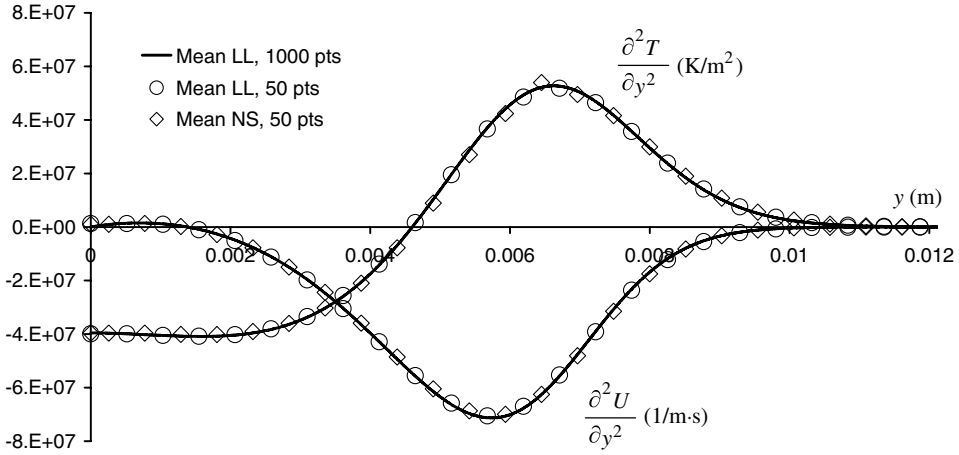

Fig. 29 Second derivatives of the profiles in Fig. 28.

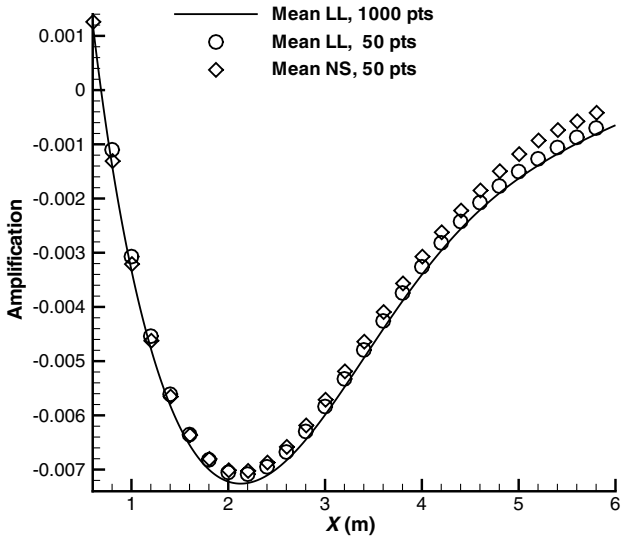

Fig. 30 Amplification rate $\alpha_i\delta^*$ for the $M^e = 2.68$ flat plate ($f = 2400$ Hz, $\psi = 69$ deg).

reference case. First-order derivatives (not shown) are very well predicted, but second-order derivatives are now distinguishable in Fig. 29.

The global impact of the method on stability results is shown in Fig. 30 for the frequency $f = 2400$ Hz. A minor difference can be observed on the amplification rate, which is consequently reported on the N factors (Fig. 31).

In fact, near-wall profiles on the vehicle forebody are even more resolved than in the test case presented above. Figure 32 reproduces the profiles of Fig. 12, the grid points being apparent, and 68 points are retained for the stability analysis. Because the main source of errors is in the finite difference derivation of the profiles before interpolation on the stability mesh, we can conclude that the overall procedure is accurate enough for the purpose of the present study.

V. Results

All the results presented hereafter are obtained in the 3a approach, using the envelope method for ψ, and concern the mixed CF/Mack's oblique first mode (of fixed frequency $f = 10$ kHz, found to be the approximately the most amplified in any case), previously referred to as mode 2 in Sec. III.D. Varying the frequency would have increased the amount of computations dramatically. The aim of the present study is, rather, to do a parametric study of the flight conditions which

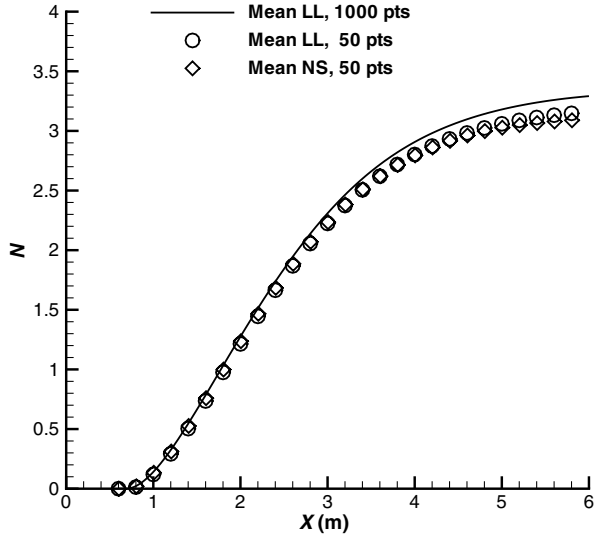

Fig. 31 Same as Fig. 30 for N factors.

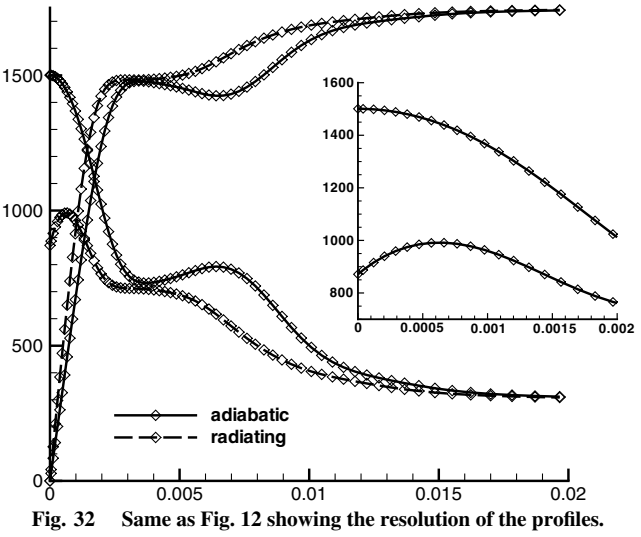

Fig. 32 Same as Fig. 12 showing the resolution of the profiles.

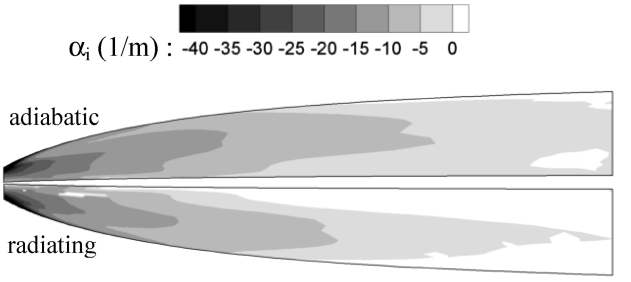

Fig. 33 Effect of the wall thermal condition on the amplification rate.

influence the transition. The parameters are 1) wall thermal condition with adiabatic or radiative equilibrium with the flow, 2) angle of attack where AOA = 2, 4, and 6 deg, and 3) a flight Mach number where $M_\infty = 4$, 6, and 8.

Indications about Mack's acoustic second mode are also given in the case $M_\infty = 8$.

A. Effect of the Wall Thermal Condition at $M = 6$ and AOA = 4 degrees

First, the effect of the wall thermal condition is investigated in the case $M = 6$, AOA = 4 deg, $f = 10$ kHz. In the adiabatic wall case, both α_i (Fig. 33) and the ψ_M angle for the most unstable wave (Fig. 34) decrease as the flow goes downstream. In particular, ψ_M values are very high close to the nose (approximately 85 deg) and weaker at the end of the forebody (approximately 70 deg). According to these values, the instabilities are first of the crossflow type, and then switch to oblique first modes in Mack's classification. Results of the radiative case confirm this observation, in agreement with classical LST results, indicating that wall cooling stabilizes the oblique first mode but has little effect on the CF waves which exist alone and then become stable at the end of the forebody. Hence, resulting N factors shown in Fig. 35 are higher in the case of an

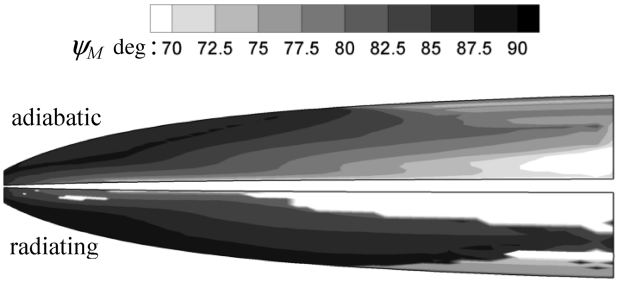

Fig. 34 Same as Fig. 33 on the most amplified wave direction.

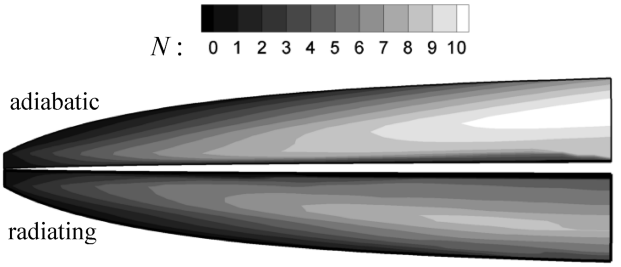

Fig. 35 Same as Fig. 33 on the *N* factors.

adiabatic wall ($N_{\max} \approx 11$) than in the case of a radiating wall ($N_{\max} \approx 8.4$). Very amplified stationary waves ($f = 0$ Hz) have also been found in some cases (not presented in this paper), which are characteristic of CF instabilities.

All the following results are now about a radiating wall, because it is more representative of flight conditions.

B. Effect of the Angle of Attack at $M = 6$

The area of interest lies in the windward side of the forebody. Increasing the angle of attack makes the BL thinner and more stable, as reported in other studies on sharp cones at the AOA (Sec. III.B). This is visible on Figs. 36–38 where the unstable region reduces as the angle of attack increases. At any AOA, ψ_M angles are always greater than 80 deg, again typical of CF instability.

The resulting *N* factors are consequently higher at small angles of attack. They reach maximum values of 9.1 at AOA = 2 deg, 8.4 at AOA = 4 deg, and 7.9 at AOA = 6 deg (Figs. 39–41), all being hardly high enough for a definite conclusion about a natural transition in flight. On the same figures the isovalues of Re_θ/M^e are plotted. Although the shape of contour lines resemble those of the *N* factors, their trend is the opposite; the higher the angle of attack, the higher the value of Re_θ/M^e at a given location. The discussion about

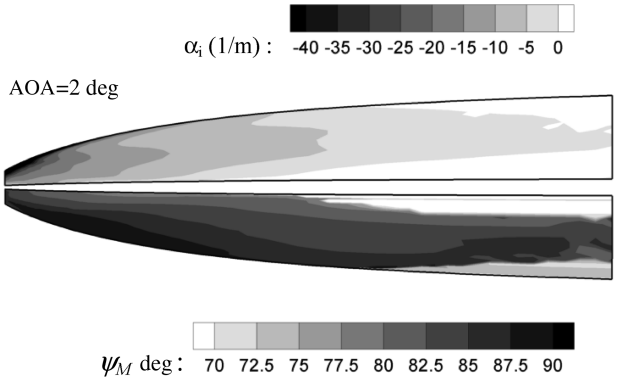

Fig. 36 Stability properties ($M_\infty = 6$, AOA = 2 deg).

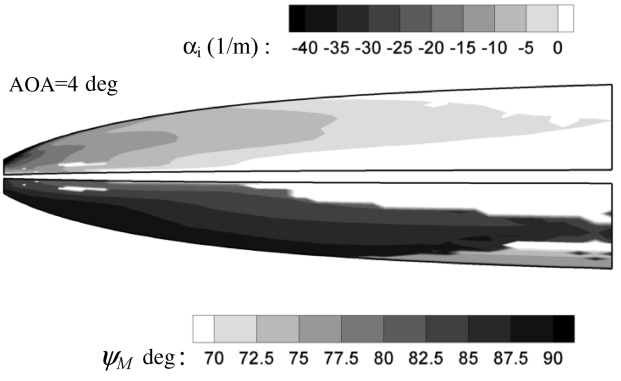

Fig. 37 Same as Fig. 36 at AOA = 4 deg.

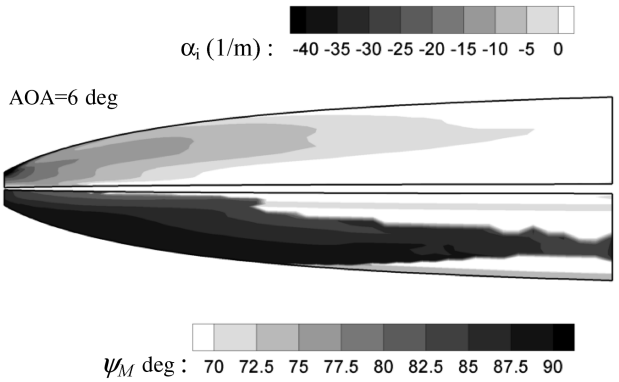

Fig. 38 Same as Fig. 36 at AOA = 6 deg.

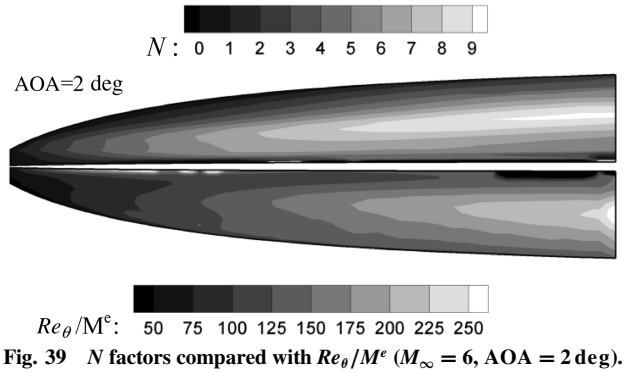

Fig. 39 *N* factors compared with Re_θ/M^e ($M_\infty = 6$, AOA = 2 deg).

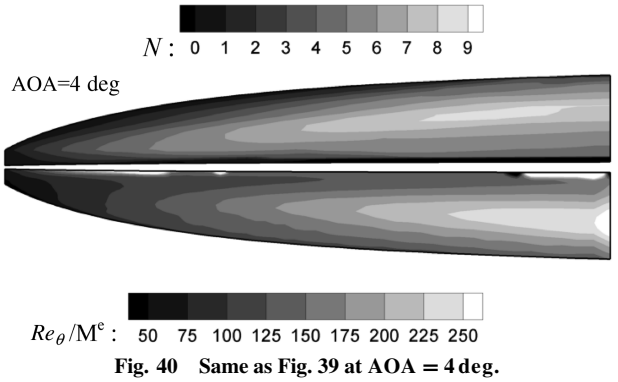

Fig. 40 Same as Fig. 39 at AOA = 4 deg.

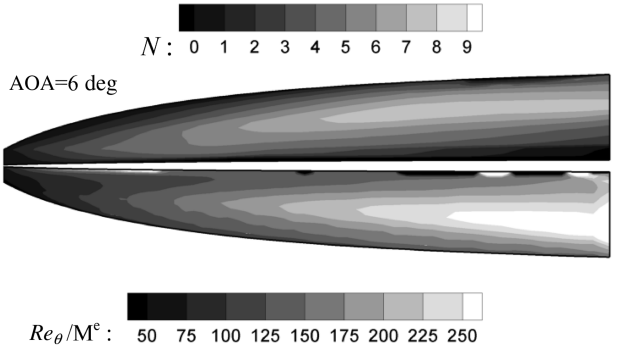

Fig. 41 Same as Fig. 39 at AOA = 6 deg.

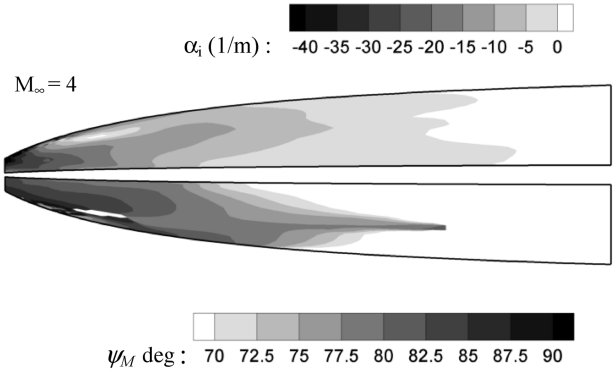

Fig. 42 Stability properties ($M_\infty = 4$ and AOA $= 4$ deg).

the significance or validity of NASP-like criterion is postponed until the next section.

C. Effect of the Mach number at AOA = 4 degrees

At Mach 4, the structure of the flow is slightly different than at Mach 6 or 8, because the shock wave is located at a greater distance from the wall. There is less pressure-driven crossflow toward the plane of symmetry, and longitudinal vortices are weaker. Instability is mainly due to oblique first modes, as observed in Fig. 42 where ψ_M values are in the range $60 \sim 80$ deg on the major part of the forebody. Amplification rates α_i are still relatively high and give N factors of the same order of magnitude as the $M_\infty = 6$ case (Fig. 43). However, the shape of N factors' contours are different because amplification rates are distributed differently and integration paths are more directed toward the centerline (black lines in Fig. 43). Crossflow instability is also found very near the nose leading edge but is of minor importance here.

On the other hand, at Mach 8, the whole forebody is dominated by crossflow instability because ψ_M is almost everywhere higher than 85 deg (Fig. 44). Corresponding N factors are shown in Fig. 45. The

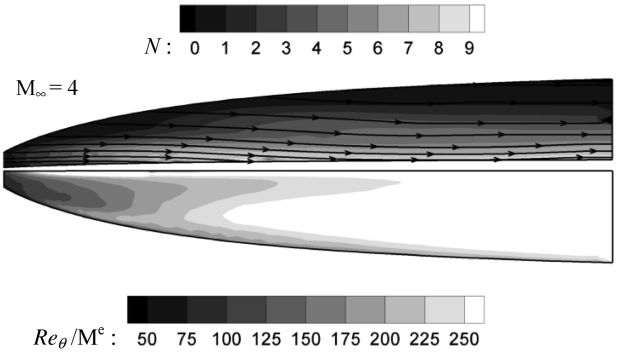

Fig. 43 N factors and integration paths compared with Re_θ/M^e ($M_\infty = 4$, AOA $= 4$ deg).

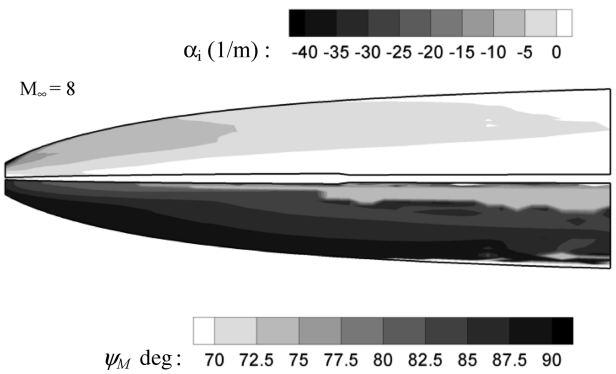

Fig. 44 Same as Fig. 42 at $M_\infty = 8$.

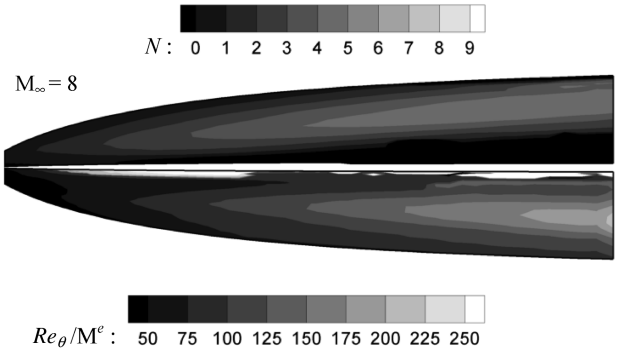

Fig. 45 Same as Fig. 43 at $M_\infty = 8$.

maximum value is 4.8, too low for a transition in flight. Contrary to the preceding case where the AOA was varying at fixed $M_\infty = 6$, a good correlation is now observed between the values of N and of Re_θ/M^e, as the flight Mach number varies from $M_\infty = 6$ to $M_\infty = 8$ at constant AOA. Reshotko [5] recently reviewed the effectiveness of the $Re_\theta/M^e = \text{Const}$ criterion for predicting transition. His conclusions are reported here. We can write

$$\frac{Re_\theta}{M^e} = \frac{\rho^e U^e \theta}{\mu^e}\frac{a^e}{U^e} = \rho^e\left(\frac{a^e\theta}{\mu^e}\right) \tag{24}$$

Both a^e and μ^e depend only on the temperature which varies slowly with the altitude, whereas ρ^e depends strongly on the pressure, hence, on the altitude. It is then obvious to observe similar evolutions for Re_θ/M^e and for the N factors which are related to the unit Reynolds number of the flow, from $M_\infty = 6$ to $M_\infty = 8$, simply because the altitude is different. Because this criterion does not take into account any physical destabilizing process, it does not work from $M_\infty = 4$ to $M_\infty = 6$. To sum up, it is questionable for cruise vehicles, but may give good results in case of reentry vehicles.

Because the Mach number outside the BL-EL is higher than 5 (see Table 1), a second acoustic two-dimensional ($\psi_M = 0$) mode also exists in the frequency range $100 \approx 300$ kHz. N factors have been calculated for several frequencies on two paths corresponding to mesh lines situated, respectively, at about one-third and two-thirds of the distance from the centerline to the external border. This mode gives N factors which do not exceed 3.5 (Fig. 46). We can conclude that in the case of a flight at $M_\infty = 8$, none of the modes that have been identified is unstable enough to provoke the natural transition by itself.

VI. Conclusions

This study has demonstrated the feasibility of applying the LST to the near-wall flow of a full-scale hypersonic vehicle, the mean-flow

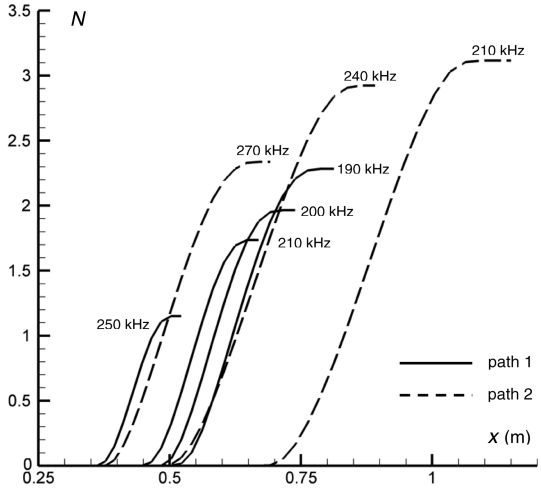

Fig. 46 N factors of Mack's second mode ($M_\infty = 8$).

Table A1 Polynomial coefficients for isobaric heat capacity of air (J/kg · K)

T, K	C_{p0}	C_{p1}	C_{p2}	C_{p3}	C_{p4}
80–1000	1005.451375	−0.039995848	8.21409×10^{-6}	4.98177×10^{-7}	-3.32144×10^{-10}
1000–6000	878.5374285	0.369200531	−0.000127397	2.05949×10^{-8}	-1.23408×10^{-12}

profiles being obtained from laminar Navier–Stokes calculations. The topology of the flow highlights two main features, including the importance of crossflow and the development of an entropy layer concentrated along the vertical plane of symmetry. Stability calculations have shown that the entropy layer induces an additional unstable mode, already identified by previous authors on canonical configurations [37]. The physical properties of this mode agree well with Lees and Lin's theory [6], and its amplification rate is quite high. Maximum related N factors are equal to four, unfortunately too weak for a natural transition in flight. Little is known about the mechanisms through which EL instability can indeed provoke transition. Further investigations, including DNS calculations, are needed to come to a conclusion.

Away from the vertical plane of symmetry, it has been shown that wall thermal conditions can change the nature of instabilities, from a combination of CF and oblique first modes in the case of a (hot) adiabatic wall to dominant CF instability in the case of a (colder) radiating wall. In the latter case, several strategies of application of the e^N criterion coupled with the envelope method for the angle of the most amplified wave have shown significant differences in the computed N factors for a given frequency. In any case, and at flight Mach numbers 4, 6, and 8, the total amplification observed is hardly high enough for a possible natural transition in flight, although destabilizing mechanisms are different. However, these results have been obtained for the single frequency $f = 10$ kHz and should be confirmed by experiments before a definite conclusion about transition. At $M_\infty = 8$, a second mode in Mack's classification has also been found, too weak again for a natural transition. Attempts to correlate computed N factors with Re_θ/M^e have been successful from $M_\infty = 6$ to $M_\infty = 8$ but have failed from $M_\infty = 4$ to $M_\infty = 6$ for reasons clearly related to the unphysical basis of this criterion [5]. The Re_θ/M^e criterion is also inadequate when the angle of attack is varied at constant M_∞. The development of a physically sound, more generally applicable criterion is presently in progress at ICARE.

Appendix: Polynomial Fits for the Thermodynamic and Transport Models

The polynomial fit for isobaric heat capacity of air is

$$C_{p,\mathrm{air}}(T) = \sum_\alpha Y_\alpha C_{p,\alpha}(T) = C_{p0} + C_{p1}T + C_{p2}T^2 + C_{p3}T^3 + C_{p4}T^4 \quad \text{(A1)}$$

The polynomial fit for viscosity $\mu(T)$ (kg/m · s) and thermal conductivity of air is

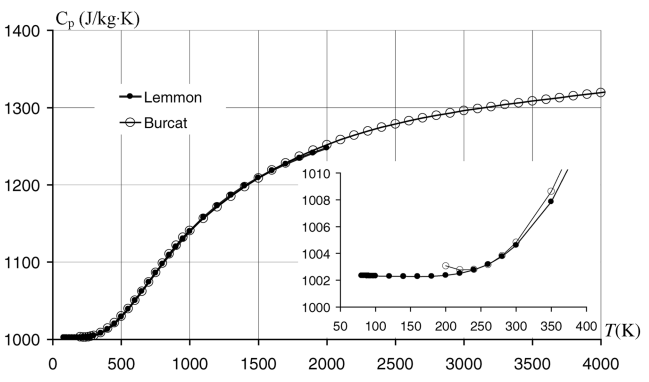

Fig. A1 Heat capacity of air.

Table A2 Polynomial coefficients for viscosity and thermal conductivity of air

Viscosity $\mu(T)$, kg/m · s	Thermal conductivity of air $k(T)$, W/m · K
$\mu_0 = 2.9141 \times 10^{-6}$	$k_0 = 5.0968 \times 10^{-3}$
$\mu_1 = 5.8921 \times 10^{-8}$	$k_1 = 7.2304 \times 10^{-5}$
$\mu_2 = -2.6383 \times 10^{-11}$	$k_2 = -8.9331 \times 10^{-9}$
$\mu_3 = 9.3607 \times 10^{-15}$	$k_3 = 7.0777 \times 10^{-13}$
$\mu_4 = -1.6670 \times 10^{-18}$	——
$\mu_5 = 1.1392 \times 10^{-22}$	——

$$\mu_{\mathrm{air}}(T) = \mu_0 + \mu_1 T + \mu_2 T^2 + \mu_3 T^3 + \mu_4 T^4 + \mu_5 T^5 \quad \text{(A2)}$$

$$k_{\mathrm{air}}(T) = k_0 + k_1 T + k_2 T^2 + k_3 T^3 \quad \text{(A3)}$$

Figure A1 gives the heat capacity of air, and Tables A1 and A2 show the polynomial coefficients for the isobaric heat capacity of air and viscosity and the thermal conductivity of air.

Acknowledgments

We thank Jean Perraud from ONERA for his helpful contribution to this work. We also thank also graduate students Romain Boré and Matthias Kraushaar who produced part of the results of Sec. V.

References

[1] Berry, S. A., DiFulvio, M., and Kowalkowski, M. K., "Forced Boundary-Layer Transition on X-43 (Hyper-X) in NASA LaRC 20-Inch Mach 6 Air Tunnel," NASA TM-2000-210316, Aug. 2000.

[2] Borg, M. P., Schneider, S. P., and Juliano, T. J., "Effect of Freestream Noise on Roughness-Induced Transition for the X-51A Forebody," AIAA Paper 2008-592, Jan. 2008.

[3] Lau, K. Y., "Hypersonic Boundary Layer Transition-Application to High Speed Vehicle Design," AIAA Paper 2007-310, Jan. 2007.

[4] Schneider, S. P., "Flight Data for Boundary Layer Transition at Hypersonic and Supersonic Speeds," *Journal of Spacecraft and Rockets*, Vol. 36, No. 1, 1999, pp. 8–20. doi:10.2514/2.3428

[5] Reshotko, E., "Is Re_θ/M^e a Meaningful Transition Criterion?," AIAA Paper 2007-943, Jan. 2007.

[6] Lees, L., and Lin, C. C., "Investigation of the Stability of the Laminar Boundary Layer in a Compressible Fluid," NACA Rept. 1115, Sept. 1946.

[7] Mack, L. M., "Linear Stability Theory and the Problem of Supersonic Boundary-Layer Transition," *AIAA Journal*, Vol. 13, No. 3, 1975, pp. 278–289. doi:10.2514/3.49693

[8] Mack, L. M., "Boundary-Layer Linear Stability Theory," AGARD Rept. 709, 1984, pp. 3-1–3-81.

[9] Malik, M. R., "Prediction and Control of Transition in Supersonic and Hypersonic Boundary Layers," *AIAA Journal*, Vol. 27, No. 11, 1989, pp. 1487–1493. doi:10.2514/3.10292

[10] Schneider, S. P., "Hypersonic Laminar-Transition on Circular Cones and Scramjet Forebodies," *Progress in Aerospace Sciences*, Vol. 40, No. 1–2, 2004, pp. 1–50. doi:10.1016/j.paerosci.2003.11.001

[11] Poll, D. I. A., "Laminar-Turbulent Transition," AGARD 319, 1996, pp. 3-1–3-20.

[12] Reshotko, E., "Transient Growth: A Factor in Bypass Transition," *Physics of Fluids*, Vol. 13, No. 5, 2001, pp. 1067–1075. doi:10.1063/1.1358308

[13] Malik, M. R., and Balakumar, P., "Acoustic Receptivity of Mach 4.5 Boundary Layer with Leading Edge Bluntness," *Theoretical and*

Computational Fluid Dynamics, Vol. 21, No. 5, 2007, pp. 323–342. doi:10.1007/s00162-007-0050-5

[14] Andersson, P., Berggren, M., and Henningson, D. S., "Optimal Disturbances and Bypass Transition in Boundary Layers," *Physics of Fluids*, Vol. 11, No. 1, 1999, pp. 134–150. doi:10.1063/1.869908

[15] Tumin, A., and Reshotko, E., "Spatial Theory of Optimal Disturbances in Boundary Layers," *Physics of Fluids*, Vol. 13, No. 7, 2001, pp. 2097–2104. doi:10.1063/1.1378070

[16] Tumin, A., and Reshotko, E., "Optimal Disturbances in Compressible Boundary Layers," *AIAA Journal*, Vol. 41, No. 12, 2003, pp. 2357–2363. doi:10.2514/2.6860

[17] Reshotko, E., and Tumin, A., "Role of Transient Growth in Roughness-Induced Transition," *AIAA Journal*, Vol. 42, No. 4, 2004, pp. 766–771. doi:10.2514/1.9558

[18] Saric, W. S., Reshotko, E., and Arnal, D., "Hypersonic Laminar-Turbulent Transition," AGARD 319, 1998, pp. 2-1–2-27.

[19] Arnal, D., "Transition Prediction in Industrial Applications," *Transition, Turbulence and Combustion Modeling*, ERCOFTAC Series, edited by A. Hanifi, P. H. Alfredsson, A. V. Johansson, and D. S. Henningson, Kluwer Academic, Norwell, MA, 1998.

[20] Vandomme, L., Chanetz, B., Benay, R., and Perraud, J., "Transitional Shock Wave Boundary Layer Interactions in Hypersonic Flow at Mach 5," AIAA Paper 2003-6966, Dec. 2003.

[21] Ferrier, M., Fedioun, I., and Davidenko, D., "Boundary-Layer Transition Prediction on a Hypersonic Vehicle Forebody," AIAA Paper 2006-8092, Nov. 2006.

[22] Burcat, A., and Ruscic, B., "Ideal Gas Thermodynamic Data in Polynomial form for Combustion and Air Pollution Use," *Third Millennium Ideal Gas and Condensed Phase Thermo Chemical Database for Combustion* [online database], http://garfield.chem.elte.-hu/Burcat/burcat.html [retrieved Dec. 2006].

[23] Lemmon, E. W., Jacobsen, R. T., Penoncello, S. G., and Friend, D. G., "Thermodynamic Properties of Air and Mixtures of Nitrogen, Argon, and Oxygen From 60 to 2000 K at Pressures to 2000 MPa," *Journal of Physical and Chemical Reference Data*, Vol. 29, No. 3, 2000, pp. 331–385. doi:10.1063/1.1285884

[24] Wilke, C. R., "A Viscosity Equation for Gas Mixtures," *Chemical Physics*, Vol. 18, No. 4, 1950, pp. 517–519. doi:10.1063/1.1747673

[25] Kee, R. J., Rupley, F. M., Miller, J. A., Coltrin, M. E., Grcar. J. F., Meeks, E., Moffat, H. K., Lutz, A. E., Dixon–Lewis, G., Smooke, M. D., Warnatz, J., Evans, G. H., Larson, R. S., Mitchell, R. E., Petzold, L. R., Reynolds, W. C., Caracotsios, M., Stewart, W. E., and Glarborg, P.*CHEMKIN Collection*, Release 3.5, Reaction Design, Inc. San Diego, CA, 1999.

[26] Malik, M. R., and Anderson, E. C., "Real Gas Effects on Hypersonic Boundary-Layer Stability," *Physics of Fluids A*, Vol. 3, No. 5, 1991, pp. 803–821. doi:10.1063/1.858012

[27] Fedorov, A., and Khokhlov, A. P., "Prehistory of Instability in a Hypersonic Boundary Layer," *Theoretical and Computational Fluid Dynamics*, Vol. 14, No. 6, 2001, pp. 359–375. doi:10.1007/s001620100038

[28] Fedorov, A., and Tumin, A., "Initial-Value Problem for Hypersonic Boundary-Layer Flows," *AIAA Journal*, Vol. 41, No. 3, 2003, pp. 379–389. doi:10.2514/2.1988

[29] Forgoston, E., and Tumin, A., "Initial-Value Problem for Three-Dimensional Disturbances in a Compressible Boundary Layer," *Physics of Fluids*, Vol. 17, No. 8, 2005, p. 084106. doi:10.1063/1.2013261

[30] Matsumura, S., and Schneider, S. P., "Streamwise Vortex Instability and Transition on the Hyper-2000 Scramjet Forebody," *Journal of Spacecraft and Rockets*, Vol. 42, No. 1, 2005, pp. 78–89. doi:10.2514/1.3959

[31] Perraud, J., Arnal, D., Dussillols, F., and Thivet, F., "Studies of Laminar-Turbulent Transition in Hypersonic Boundary Layers at ONERA," *Proceedings of the 3rd European Symposium for Aerothermodynamics for Space Vehicles*, ESTEC, Noordwijk, The Netherlands, Nov. 1998, p. 309.

[32] Kimmel, R. L., Klein, M. A., and Schwoerke, S. N., "Three-Dimensional Hypersonic Laminar Boundary-Layer Computations for Transition Experiment Designs," *Journal of Spacecraft and Rockets*, Vol. 34, No. 4, July–Aug. 1997, pp. 409–415. doi:10.2514/2.3236

[33] Kimmel, R. L., Poggie, J., and Schwoerke, S. N., "Laminar-Turbulent Transition in a Mach 8 Elliptic Cone Flow," *AIAA Journal*, Vol. 37, No. 9, Sept. 1999, pp. 1080–1087. doi:10.2514/2.836

[34] Stetson, K. F., and Rushton, G. H., "Shock Tunnel Investigation of Boundary-Layer Transition at $M = 5.5$," *AIAA Journal*, Vol. 5, No. 5, 1967, pp. 899–906. doi:10.2514/3.4098

[35] Fedorov, A., and Tumin, A., "Evolution of Disturbances in Entropy Layer on Blunted Plate in Supersonic Flow," *AIAA Journal*, Vol. 42, No. 1, 2004, pp. 89–94. doi:10.2514/1.9033

[36] Maslov, A. A., Shiplyuk, A. N., Bountin, D. A., and Sidorenko, A. A., "Mach 6 Boundary-Layer Stability Experiments on Sharp and Blunted Cones," *Journal of Spacecraft and Rockets*, Vol. 43, No. 1, 2006, pp. 71–76. doi:10.2514/1.15246

[37] Dietz, G., and Hein, S., "Entropy-Layer Instabilities Over a Blunted Flat Plate in Supersonic Flow," *Physics of Fluids*, Vol. 11, No. 1, 1999, pp. 7–9. doi:10.1063/1.869899

[38] Brinich, P. F., "Effects of Leading-Edge Geometry on Boundary Layer Transition at Mach 3.1," NACA 3659, 1956.

[39] Cebeci, T., and Stewartson, K., "On Stability and Transition in Three-Dimensional Flows," *AIAA Journal*, Vol. 18, No. 4, 1980, pp. 398–405. doi:10.2514/3.50772

[40] Nayfeh, A. H., "Stability of Three-Dimensional Boundary Layer," *AIAA Journal*, Vol. 18, No. 4, 1980, pp. 406–416. doi:10.2514/3.50773

[41] Mack, L. M., "Stability of Three-Dimensional Boundary Layers on Swept Wings at Transonic Speeds," *IUTAM Symposium on Transonicum III*, edited by J. Zierep, and H. Oertel, Springer–Verlag, New York, 1988.

R. Kimmel
Associate Editor